

Membraneless channels sieve cations in ammonia-oxidizing marine archaea

<https://doi.org/10.1038/s41586-024-07462-5>

Received: 13 January 2023

Accepted: 24 April 2024

Published online: 29 May 2024

Open access

 Check for updates

Andriko von Kügelgen^{1,2}, C. Keith Cassidy³, Sofie van Dorst², Lennart L. Pagani², Christopher Batters⁴, Zephyr Ford², Jan Löwe¹, Vikram Alva⁵, Phillip J. Stansfeld⁶ & Tanmay A. M. Bharat^{1✉}

Nitrosopumilus maritimus is an ammonia-oxidizing archaeon that is crucial to the global nitrogen cycle^{1,2}. A critical step for nitrogen oxidation is the entrapment of ammonium ions from a dilute marine environment at the cell surface and their subsequent channelling to the cell membrane of *N. maritimus*. Here we elucidate the structure of the molecular machinery responsible for this process, comprising the surface layer (S-layer), using electron cryotomography and subtomogram averaging from cells. We supplemented our in situ structure of the ammonium-binding S-layer array with a single-particle electron cryomicroscopy structure, revealing detailed features of this immunoglobulin-rich and glycan-decorated S-layer. Biochemical analyses showed strong ammonium binding by the cell surface, which was lost after S-layer disassembly. Sensitive bioinformatic analyses identified similar S-layers in many ammonia-oxidizing archaea, with conserved sequence and structural characteristics. Moreover, molecular simulations and structure determination of ammonium-enriched specimens enabled us to examine the cation-binding properties of the S-layer, revealing how it concentrates ammonium ions on its cell-facing side, effectively acting as a multichannel sieve on the cell membrane. This in situ structural study illuminates the biogeochemically essential process of ammonium binding and channelling, common to many marine microorganisms that are fundamental to the nitrogen cycle.

The ocean is our planet's largest biome, where pelagic microbial Thaumarchaeota (syn. Nitrososphaerota) represent one of the most abundant organisms³. The numerical dominance of marine thaumarchaea suggests that they have a major role in global biogeochemical cycles^{1,2}. *N. maritimus*, an intensely studied marine thaumarchaeon, grows chemolithoautotrophically by aerobically oxidizing ammonia to nitrite⁴. This organism has also been shown to regenerate oxygen under anoxic conditions, and to fix CO₂^{4,5}, placing it in an important position in the global nitrogen and carbon dioxide biogeochemical cycles.

Owing to the low concentration of ammonia (NH₃) or ammonium (NH₄⁺) ions in the oceans, reported in the 10⁻⁸ to 10⁻⁹ M range⁶, marine archaea such as *N. maritimus* have evolved specialized molecular machinery to attract ammonium ions on their cell surface to facilitate ammonium oxidation at the cell membrane⁷. *N. maritimus*, like most archaeal cells, is encased by a paracrystalline, proteinaceous surface layer or S-layer⁸⁻¹¹. Bulk modelling of the *N. maritimus* S-layer has predicted that this cellular organelle might have a key role in elevating the ammonium concentrations in the pseudoperiplasmic space between the S-layer and the cell membrane^{12,13}; however, how this occurs on a mechanistic and molecular level is unclear. At the overall morphological scale, the *N. maritimus* S-layer has been reported to have a hexagonal arrangement^{9,12} and is postulated to consist of repeating subunits of the proteins Nmar_1547 or Nmar_1201 (two proteins with 91% sequence

identity), based on transcriptomic and proteomic data^{14,15}. Here, to understand the rules governing ammonium binding and enrichment by *N. maritimus* and related marine Thaumarchaeota, we investigated the molecular structure of the *N. maritimus* S-layer using structural, biochemical, cellular and bioinformatic methods.

Cryo-ET analysis of the *N. maritimus* S-layer

To gain insights into this problem, we used electron cryotomography (cryo-ET) and subtomogram averaging techniques. We have previously applied these methods to determine in situ structures of prokaryotic S-layers from in vitro purified specimens containing cellular fragments¹⁶⁻¹⁸. Our goal was to solve the structure of the *N. maritimus* S-layer directly from whole cells. Cryo-ET analysis of *N. maritimus* cells revealed an S-layer surrounding the approximately 300-nm-wide elongated cells, which contained a compact nucleoid and several cytosolic ribosomes (Fig. 1a). Using subtomogram averaging, we mapped the locations of the S-layer repeating units on the cell, which were arranged in a hexagonal array (Fig. 1b). We found that the S-layer hexamers coated the cells with near-perfect continuity along their lengths, while local pentameric defects were present on the cell edges, completing the S-layer (Fig. 1b), which was confirmed by quantification of hexamer and pentamer positions relative to the centre of the cell (Fig. 1c).

¹Structural Studies Division, MRC Laboratory of Molecular Biology, Cambridge, UK. ²Sir William Dunn School of Pathology, University of Oxford, Oxford, UK. ³Department of Physics and Astronomy, University of Missouri-Columbia, Columbia, MO, USA. ⁴Protein and Nucleic Acid Chemistry Division, MRC Laboratory of Molecular Biology, Cambridge, UK. ⁵Department of Protein Evolution, Max Planck Institute for Biology Tübingen, Tübingen, Germany. ⁶School of Life Sciences and Department of Chemistry, University of Warwick, Coventry, UK. ✉e-mail: tbharat@mrc-lmb.cam.ac.uk

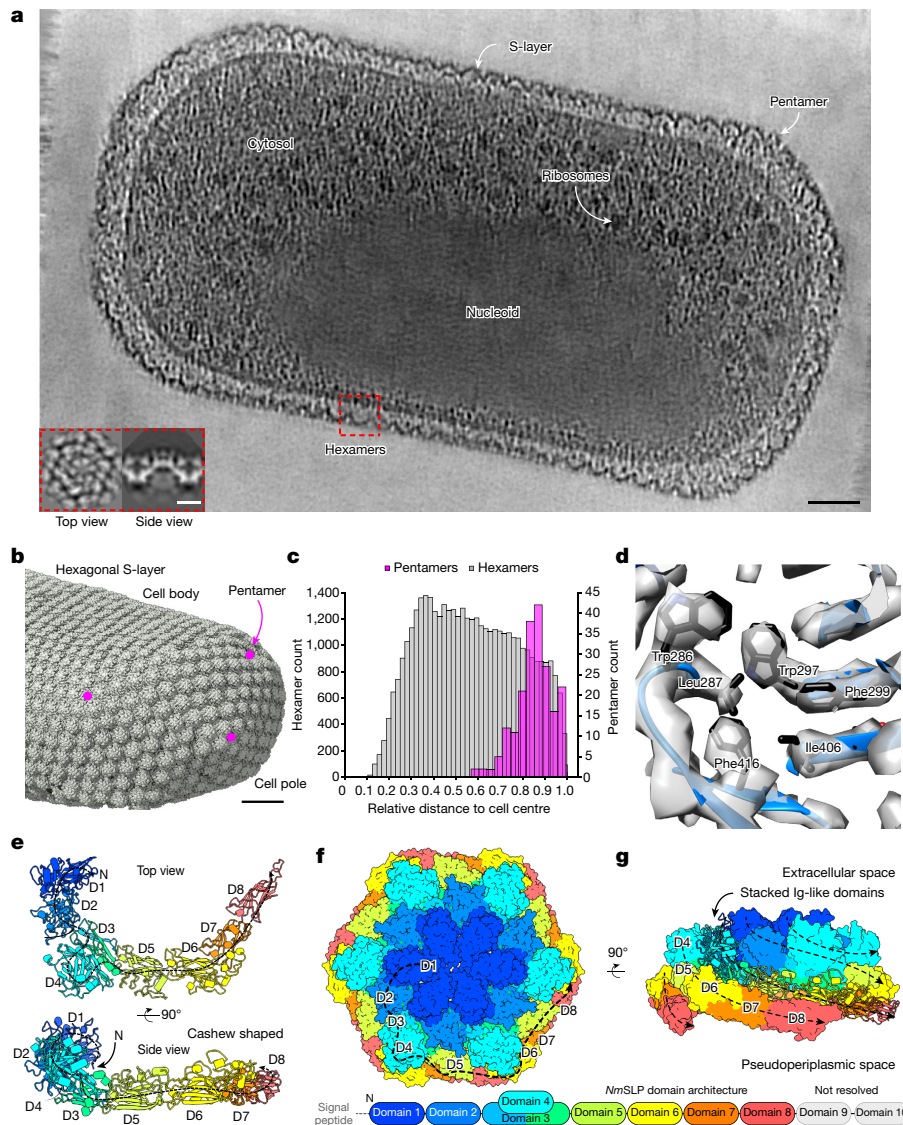


Fig. 1 | The molecular structure and assembly of the *N. maritimus* S-layer in intact cells. **a, A denoised^{36,37} tomographic slice through a *N. maritimus* cell shows ultrastructural details of this marine archaeon (annotated). Inset: top and side views of the subtomogram average of the S-layer. Scale bars, 500 Å (main image) and 100 Å (inset). Cellular tomography was performed at least 27 times (Extended Data Table 1). **b**, Map of the subtomogram positions in the cellular S-layer showing the presence of pentameric defects at the edge of the cell. Scale bar, 500 Å. **c**, A histogram of subtomogram positions from all tomograms relative to the three-dimensional centre of the cell body ($n = 41,303$**

hexamers (grey) and $n = 203$ pentamers (pink); one out of two biological replicates shown). **d**, The subtomogram averaging map enables derivation of a molecular model directly from cellular data. Amino acid residue side chains resolved are marked. See also Extended Data Figs. 1 and 2. **e**, A ribbon model of the cashew-shaped *NmSLP* monomer is shown in two orthogonal views. **f, g**, The structure of the S-layer hexamer displayed in two orthogonal views shows that *NmSLP* monomers are arranged as an array of Ig-like domains; each domain (D) is coloured differently (a schematic is shown below). The first eight Ig-like domains are resolved in the cryo-ET and subtomogram averaging map.

Next, we used state-of-the-art cryo-ET imaging and image-processing workflows, which have been shown to support high-resolution in situ structure determination from purified specimens¹⁹. As a result, we produced a high-resolution map of the *N. maritimus* S-layer hexamer from intact cells (Fig. 1d, Extended Data Fig. 1, Extended Data Table 1 and Supplementary Videos 1 and 2). The central region of the S-layer hexamer in the map had a resolution of 3.3 Å, with the resolution decaying to around 4.5 Å towards the periphery (Extended Data Fig. 1). The subtomogram averaging map contained sufficient details to enable us to derive an atomic model of the S-layer (Fig. 1d–g and Extended Data Fig. 2). The structure shows that the S-layer is pseudohexagonal (Fig. 1f,g) and consists of the repeated interactions of the Nmar_1547 (hereafter, *NmSLP*) S-layer protein. Despite the high sequence similarity of *NmSLP* to the other previously predicted SLP, Nmar_1201, a unique segment of *NmSLP* between residues 911 and 977 was clearly resolved

in our map. This enabled us to identify *NmSLP* as the primary *N. maritimus* SLP on cells through direct structure determination (Extended Data Fig. 2). This observation confirms previous transcriptomic data showing high expression levels of the *Nmar_1547* gene compared with *Nmar_1201*¹⁴. However, we cannot rule out that Nmar_1201 could be present at lower copy numbers.

At the sequence level, *NmSLP* is arranged into ten immunoglobulin-like (Ig-like) domains (Fig. 1f,g). The first eight domains were well resolved in our 3.3–4.5-Å-resolution subtomogram averaging map. By contrast, the last two domains appeared less ordered, with the local resolution decaying towards the C terminus of *NmSLP*, away from the centre of the S-layer hexamer (Extended Data Figs. 1 and 2). At the N terminus, the C_6 symmetry of the hexamer is broken, revealing a distinctly two-fold symmetric central pore (Extended Data Fig. 2). Each monomer of *NmSLP* in the S-layer adopts a rough 'cashew' shape, facilitating

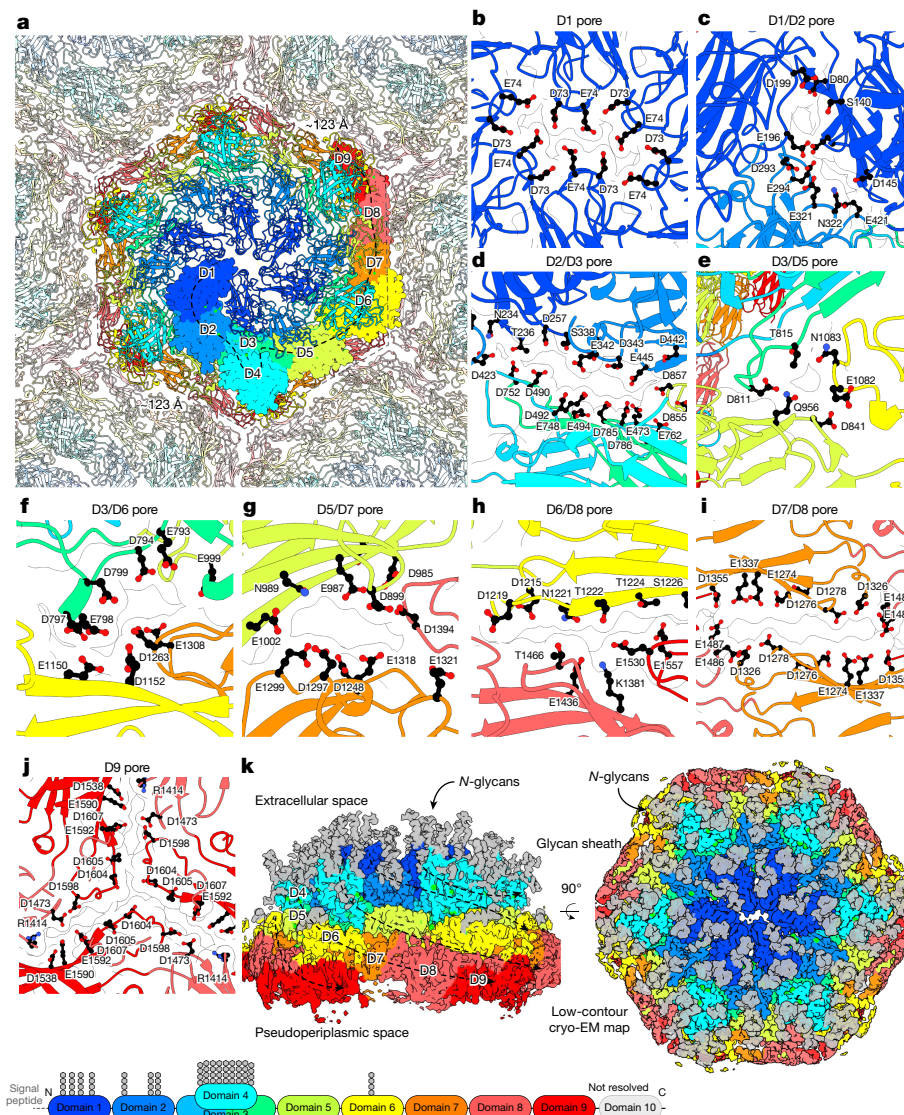


Fig. 2 | Cryo-EM structure of isolated *N. maritimus* S-layer sheets. **a**, In vitro cryo-EM structure (global resolution, 2.7 Å) of isolated S-layer sheets from *N. maritimus*. The colour scheme for ribbon diagrams is the same as in Fig. 1; domains of one NmSLP are marked. **b–j**, Magnified views of the pores lined with negatively charged residues, which are ubiquitous in the S-layer sheet.

several interactions around the hexamer of NmSLP (Fig. 1e–g). Domain 4, nestled within domain 3 and linked by short connectors, is slightly raised relative to the base of the cashew-shaped Ig-array of NmSLP, projecting towards the extracellular milieu.

Although the amino acid residues (37–1499) from the first eight Ig-like domains could be unambiguously built into the subtomogram averaging map, several unexplained densities were observed, emanating from surface-exposed asparagine residues (Extended Data Fig. 2). Given that archaeal SLPs are known to be heavily glycosylated²⁰, we hypothesized that these densities might correspond to glycans. Another notable set of unexplained densities was observed near the negatively charged amino acid residue side chains of Asp73 and Glu74 at the central C₂ pore, as well as between NmSLP monomers around the hexamer (Extended Data Fig. 2). Considering that positively charged ions have been previously observed bound to S-layers^{21,22}, we hypothesized that these additional densities on the *N. maritimus* S-layer could potentially correspond to bound cations, although the resolution of the map prevented us from unambiguously assigning their chemical identities.

The location of the pores is given in the titles of the panels. **k**, The sharpened cryo-EM map shows 17 glycans decorating each NmSLP; the map shown at a lower contour level in two different orientations. A schematic of the glycan locations on the NmSLP sequence is shown below.

Cryo-EM shows a porous S-layer

The *N. maritimus* S-layer has previously been predicted through bulk biophysical modelling to help attract ammonium ions¹². Considering the tight sheath formed by the S-layer around cells (Fig. 1b,c), providing an extremely large surface area for interaction with the marine environment, we postulated that the S-layer functions as a negatively charged ammonium trap. This would facilitate the movement of cations such as ammonium towards the cell membrane, specifically to the sites of ammonium oxidation. To test these hypotheses with higher resolution structures, in which ion and other densities would be better resolved, we purified *N. maritimus* cell envelopes for cryo-electron microscopy (cryo-EM) analysis. We then used single-particle techniques, as applied previously to two-dimensional S-layer sheets for structure determination^{18,23}, to solve a 2.7-Å-resolution structure of the S-layer (Fig. 2a, Extended Data Fig. 3 and Extended Data Table 2).

The single-particle structure was very similar (root mean squared deviation of 2.21 Å for the full composite model, 0.54 Å for residues 35–455 (refined in C₂) and 1.39 Å for residues 466–1498 (refined in C₁))

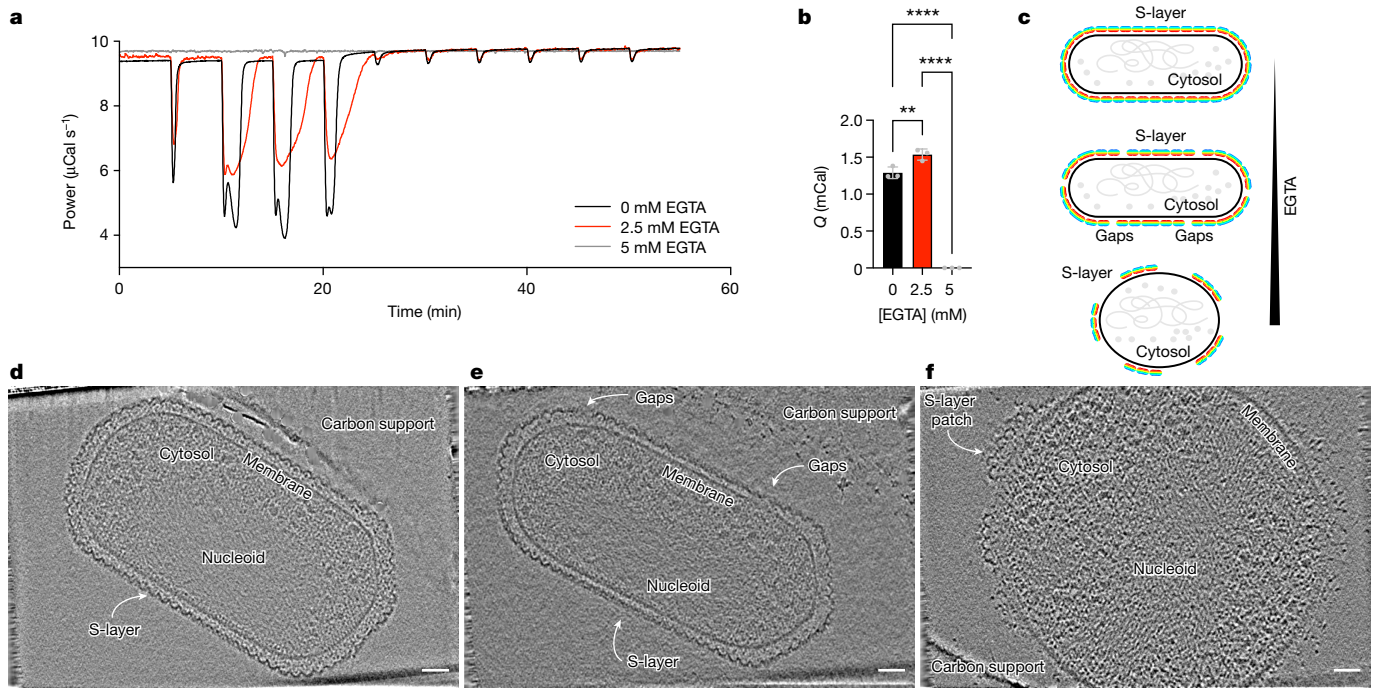


Fig. 3 | Ammonium ions either bind directly to the S-layer or pass through it to bind to the underlying cell. a, ITC signal of intact *N. maritimus* cells titrated with ammonium chloride with different pretreatments with EGTA. **b**, Quantification of the ITC curves showing the total heat (Q) released in the different experiments. Data are mean \pm s.d. $n = 3$ biologically independent replicates. Statistical analysis was performed using ordinary one-way analysis of variance (ANOVA) with correction for multiple comparisons; **** $P < 0.0001$, ** $P = 0.0075$. **c**, Schematic of the ITC and cryo-ET experiment presented.

d, Cryo-ET analysis of *N. maritimus* cells after titration with ammonium chloride shows complete coating with an S-layer. $n = 150$ from two biological replicates. **e**, Cryo-ET analysis of *N. maritimus* cells treated with 2.5 mM EGTA after titration with ammonium chloride shows gaps in the S-layer in a heterogeneous cell population. $n = 83$ from two biological replicates. **f**, Cryo-ET analysis of *N. maritimus* cells treated with 5 mM EGTA after titration with ammonium chloride showing round cells with a naked membrane. $n = 152$ from three biological replicates. For **d–f**, scale bars, 500 Å.

to the subtomogram averaging structure (Fig. 2, Extended Data Fig. 4 and Supplementary Video 3), enabling us to extend our structure by modelling the ninth Ig-like domain, reaching up to residue 1616 out of 1734 (Fig. 2a and Extended Data Fig. 3). The last Ig-like domain remains unresolved in our map, with only disordered, diffuse density observed beyond the ninth Ig-like domain of *NmSLP* in the pseudoperiplasmic space, indicating flexibility relative to the rigid part of the S-layer. The *NmSLP* hexamer in the single-particle structure appears to be slightly expanded compared with the subtomogram averaging structure (Supplementary Video 3), perhaps due to differences in the S-layer curvature.

The *N. maritimus* genome also encodes a homologue for a cell-anchoring SlaB protein (Extended Data Fig. 5a,b and Supplementary Table 1) that is known to bind the S-layer of the archaeon *Sulfolobus acidocaldarius* to the cell membrane²⁴. However, proteomic data on *N. maritimus* indicate that this protein is considerably less abundant in the cell than *NmSLP*¹⁵. We speculate that the last (tenth), unresolved Ig-like domain of *NmSLP* may have a role in anchoring the S-layer to molecules present on the cell envelope, therefore partially reducing the need for stoichiometric anchoring by a SlaB or a SlaB-like protein in *N. maritimus*.

In our single-particle structure, the subunit contacts between *NmSLP* hexamers (Fig. 2b–j) were better resolved compared with in our subtomogram averaging map (Fig. 1). Notably, several contact sites, both between hexamers and within each hexamer, contain pores lined predominantly by rows of negatively charged amino acid residues (Fig. 2b–j). These pores are relatively small (around 5 Å) but are compatible with the size of small chemical species, fitting with the idea that the pores of the S-layer may function as cation channels. Owing to the repeating pattern of the S-layer, these pores span the entirety of the *N. maritimus* cell surface. Supporting the anticipated cation-binding

properties of the S-layer, a bioinformatics comparison of the amino acid composition of *NmSLP* with that of the *N. maritimus* proteome and all archaeal proteins revealed a substantial increase in aspartic acid residues (10.9% in *NmSLP* versus 6.1% in the *N. maritimus* proteome versus 7.3% in all archaea). Concurrent with this, the percentages of lysine and arginine residues are reduced (1.7% and 2.2% in *NmSLP* versus 8.4% and 3.4% in the *N. maritimus* proteome versus 3.8% and 5.9% in all archaea), resulting in an S-layer that is highly negatively charged.

Overall, our structure shows that the *NmSLP* monomers densely populate the S-layer sheet. This arrangement is reminiscent of the S-layer in the Dead Sea archaeon *Haloferax volcanii*, which is composed of an SLP called *csg*, which also consists of tandemly repeated Ig-like domains¹⁸. Such arrays of Ig-like domains have been observed in archaeal^{18,25}, monoderm bacterial^{22,26} and diderm bacterial S-layers^{23,27}. Although these SLPs share some structural similarities, they diverge notably at the sequence level, as well as at the overall organizational level containing different number of domains (Extended Data Fig. 5c), enabling them to assemble into unique two-dimensional sheets^{23,24}, each with distinctly different glycosylation patterns and cell anchoring mechanisms.

In total, 17 glycan densities per monomer of *NmSLP* were also resolved in the single-particle map (Fig. 2k and Extended Data Fig. 4). Although these densities do not support direct derivation of the chemical structure of the glycans, they project away from the cell surface at asparagine residues, which are followed by a threonine or serine residue at the +2 position (Fig. 2k). Enshrouding the outer domains of the proteinaceous *NmSLP* S-layer, these glycans form a thick shell, encasing the cell in a sugar-rich coat (Fig. 2k). The mesh-like arrangement of the glycans probably provides protection, potentially shielding the cell from phages²⁸. It might also enhance the hydrophilicity of the cell surface, making it suitable for marine environments. Most of these glycans are

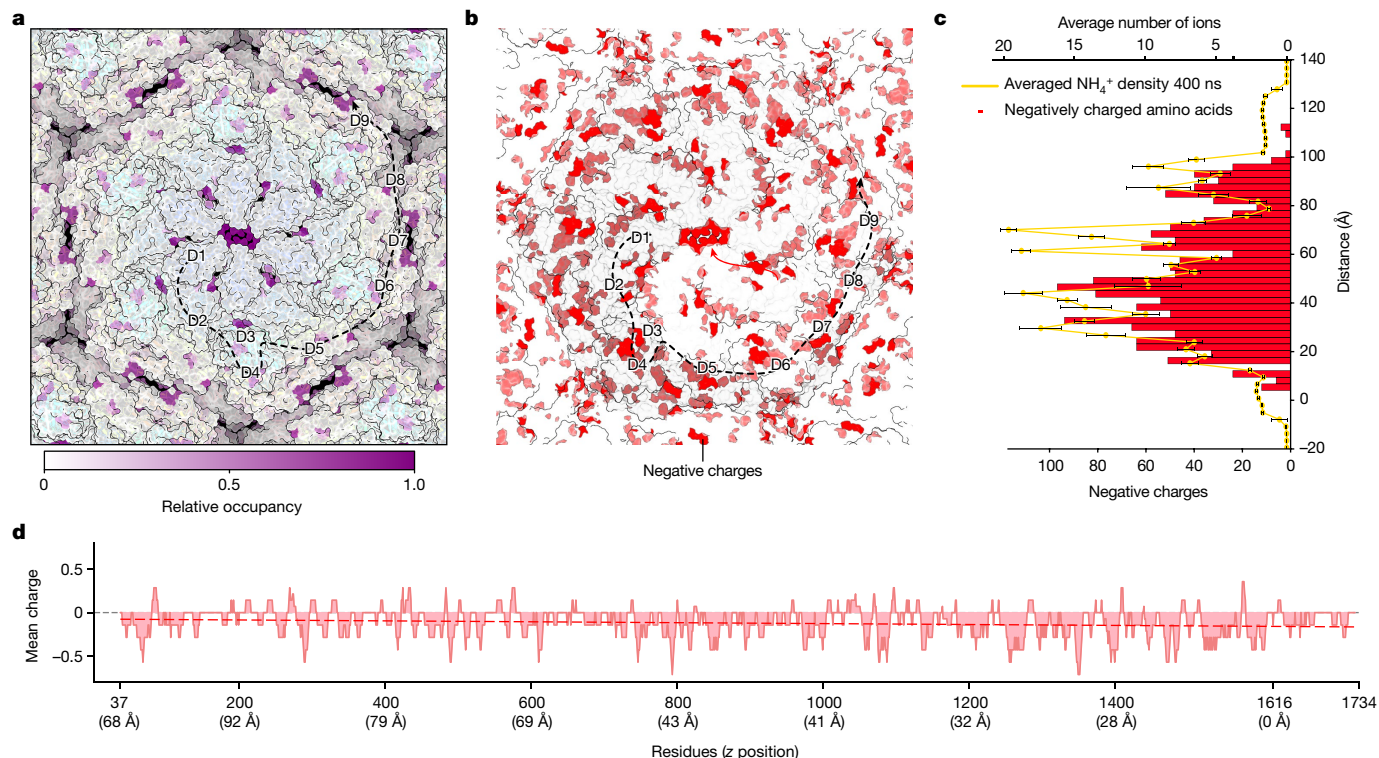


Fig. 4 | Ammonium (NH_4^+) binding to the negatively charged S-layer lattice.

a, MD simulations support ammonium-ion binding at the S-layer pores. Residue-based ammonium occupancies during the 0.1 M NH_4^+ MD simulations are plotted onto the S-layer structure on a relative scale from white to purple.

b, The distribution of negatively charged residues (shown in red) in the S-layer matches well with the MD simulations showing predicted ammonium-binding residues (Extended Data Fig. 6). **c**, A histogram of negatively charged residues along the S-layer, overlaid onto the ammonium-ion positions in the 0.1 M NH_4^+

MD simulations (distance was calculated from the closest, membrane-proximal amino acid residue in the S-layer structure). For the averaged ammonium-ion residence from three independent MD simulations (averaged over the last 400 ns of each simulation), the error bars denote ± 1 s.d. (Supplementary Fig. 2). **d**, The mean local charge of *NmSLP* plotted along the sequence shows a gradual but continual increase in negative charge. The z position of the *NmSLP* residues, derived from the S-layer structure, is indicated, with the ninth Ig-like domain forming the base of the S-layer, proximal to the cell membrane.

located in the N-terminal segment of *NmSLP*, primarily in outermost domains 1, 2 and 4, with a single glycan present in domain 6 (Fig. 2k).

Ammonium binding of the S-layer

We confirmed that the concentration of ammonium ions in the medium strongly influences the growth of *N. maritimus* (Supplementary Fig. 1a), as shown previously^{4,9}. To directly measure ammonium ion binding to the cell surface, we performed isothermal titration calorimetry (ITC), titrating a medium containing NH_4Cl against whole *N. maritimus* cells. As expected, growing *N. maritimus* cells showed strong and robust ammonium binding (Fig. 3a,b and Supplementary Fig. 1b; $n = 3$). We subsequently performed cryo-ET analysis of the same sample after ITC measurements, revealing normal cell morphology with an intact S-layer coating the cells (Fig. 3c,d; $n = 150$). As ammonium is the sole energy source for these growing cells, ammonium ions must somehow reach the cell for oxidation; we therefore inferred that the measured ammonium binding occurs either directly to the S-layer or to the underlying cell after passage through the S-layer (Fig. 3c,d). We then perturbed the S-layer by pretreating the cells with ethylene glycol-bis(β -aminoethyl ether)-*N,N,N',N'*-tetraacetic acid (EGTA), which is known to impair several prokaryotic S-layers¹⁶. *N. maritimus* cells that were pretreated with 2.5 mM EGTA showed altered ammonium binding (Fig. 3a,b and Supplementary Fig. 1b; $n = 3$), concurrent with observed gaps and partial S-layer disruptions seen in cryo-ET in a heterogeneous population (Fig. 3e; $n = 83$). Near-complete disruption of the S-layer with 5 mM EGTA entirely abolished ammonium binding (Fig. 3a,b and Supplementary Fig. 1b; $n = 3$), leading to rounding up

of cells with exposed, uncoated membranes (Fig. 3f; $n = 152$). These experiments indicate that an intact S-layer is critical for ammonium binding and may also be important for cell shape maintenance in *N. maritimus* in a calcium-dependent manner.

To examine the biochemically observed ammonium-binding properties of the S-layer structurally, we purified S-layer sheets *in vitro*, at a higher concentration of ammonium (2.5 mM compared to 1 mM NH_4Cl) and resolved a 3.1-Å-resolution cryo-EM structure of the S-layer enriched in ammonium ions. Compared with our original cryo-ET structure (Supplementary Fig. 1c–f), this ammonium-enriched S-layer structure showed an increased number of unexplained densities at several S-layer pores, indicative of ammonium ion binding to the negatively charged amino acid residues lining these pores (Supplementary Fig. 1c–f).

To further investigate the ability of the lattice to bind to cations, we performed atomistic molecular dynamics (MD) simulations of the *N. maritimus* S-layer in the presence of ammonium (Fig. 4a, Methods, Extended Data Fig. 6 and Supplementary Fig. 2), using a framework that has recently been shown to yield strong agreement with X-ray crystallography and cryo-EM studies of cation binding to S-layers²¹. Analysis of residue-based ammonium occupancies over the course of three 500 ns simulations using PyLipID²⁹ clearly identified the primary acidic residues that mediate ammonium binding (Supplementary Table 2 and Supplementary Video 4). Moreover, mapping the high-ammonium occupancy (>50%) residues onto the hexamer structure revealed multiple acidic residue clusters in excellent agreement with the pores identified in our cryo-EM and cryo-ET maps (Fig. 4b and Extended Data Fig. 7). These observations are compatible with the idea that the

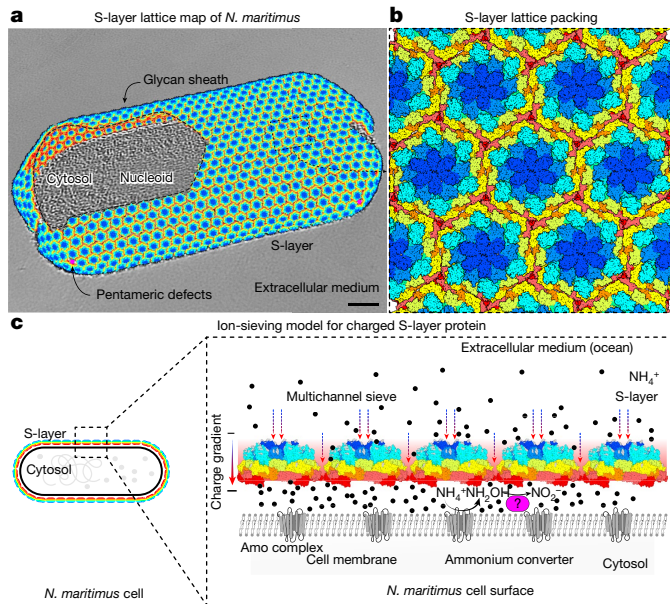


Fig. 5 | The in situ structure of the *N. maritimus* S-layer shows a multichannel sieve nearly perfectly coating cells at high-copy numbers. **a**, The S-layer lattice coats nearly the entire outer surface of *N. maritimus* cells. A small part of the lattice map (black dashed line) has been cut out from the top of the cell for clarity. The pseudohexagonal lattice is joined together by pentameric defects (Extended Data Fig. 8). Scale bar, 500 Å. Cellular tomography was performed at least 32 times (Extended Data Table 1). **b**, A model of the S-layer lattice is shown as a space-filling representation with the same colour scheme as in Fig. 1. **c**, The ion-exchanging model for the *N. maritimus* S-layer. The highly negatively charged S-layer entraps ammonium ions, and these ions may move along multiple pores in the lattice, aided by increasing negative charge along the lattice. Once beyond the S-layer, the ammonium ions can diffuse to the membrane predominantly composed of crenarchaeol³⁹, where they are converted to nitrite through hydroxylamine (NH₂OH) as an intermediate by an unknown protein complex (pink)³⁴, setting up an ion sink and concentration gradient between the S-layer and the membrane.

multiple pores in the S-layer sheet, lined with negatively charged residues, facilitate the movement of ammonium ions across the S-layer. Furthermore, in our simulations, we also found that ammonium ions could be replaced with sodium ions, suggesting that the S-layer might not discriminate between different small positively charged ions for binding (Supplementary Fig. 2).

Collectively, our structural data reveal that the S-layer of *N. maritimus* functions as a multichannel exchanger for ammonium ions, featuring negatively charged residues that line several pores in the S-layer (Fig. 2b–j). In this context, it is interesting that the negative charge of the S-layer increases when moving from the extracellular environment toward the cell membrane (Fig. 4c), specifically from the N to the C terminus of each *NmSLP*. This charge gradient probably facilitates the movement of ammonium ions through the S-layer towards the cell membrane. Our MD simulations support this hypothesis, showing an accumulation of ammonium ions at the cell-facing side of the S-layer (Fig. 4c, Supplementary Fig. 2 and Supplementary Video 4). To ensure that these observations did not depend on the amount of ammonium present, we conducted further MD simulations of the S-layer system in 0.05 M or 0.2 M ammonium, reproducing in both cases strong ammonium binding by the S-layer and relative accumulation of ammonium ions towards the cell-facing side of the S-layer (Supplementary Fig. 2).

The observed increase in negative charge at the structural level is also mirrored at the sequence level. There is a continuous and substantial increase in negative charge from the N to the C terminus of

the *NmSLP* protein sequence (Fig. 4d), with the membrane-proximal C terminus being highly negatively charged. Using sensitive sequence-based homology searches and structure prediction, we found that Ig-domain-containing SLPs with a charge gradient are common across all described groups of ammonia-oxidizing archaea (AOA), suggesting similar S-layer arrangements in these species (Extended Data Fig. 7). Although the overall domain organization of such AOA and other archaeal SLPs could be similar (Extended Data Fig. 5a,b), the number of Ig-like domains and the charge distribution in each SLP vary, possibly reflecting differences in the function of these S-layers in binding positively charged molecules and ions (Extended Data Fig. 7d).

Molecular modelling of the cell surface

Together, our data enabled us to construct a molecular model of the *N. maritimus* cellular S-layer (Fig. 5a,b). Subtomogram position mapping of the S-layer hexamers and pentamers demonstrates that the S-layer coats the cell surface with near-perfect continuity (Fig. 5a,b), a characteristic that is also observed in other archaeal S-layers¹⁸. The continuous S-layer is heavily glycosylated, possibly protecting the cell from phages in the harsh marine environment. The dome-shaped structure of the S-layer hexamer probably supports flexibility, allowing *NmSLP* to coat different parts of the cell membrane with varied curvature. The S-layer is closed around cells by pentameric positions, which also appear to be composed of *NmSLP* (Extended Data Fig. 8). At the technical level, this study highlights the power of modern structural biology—molecular structures obtained from whole-cell cryo-ET, in conjunction with in-cell biochemistry and MD simulations, can provide key biochemical and mechanistic insights. With advancements in data collection and image-processing methodologies^{19,30,31}, we anticipate that such in situ structural techniques will significantly enhance our molecular understanding of cells (Supplementary Fig. 3).

Conclusion

Our data are consistent with a scenario in which ammonium and other cations are bound and enriched at the cell surface by the negatively charged S-layer (Fig. 5c). The S-layer provides an extremely large surface area for interaction with the surrounding marine environment, where it acts as a multichannel cation exchanger and, due to its gradually increasing negative charge, leads to the accumulation of ammonium ions on the cell-facing side of the S-layer. An ‘ammonium sink’ exists at the cell membrane, where the integral membrane machinery, ammonia monooxygenase^{32,33}, converts NH₄⁺ to NO₂⁻ with hydroxylamine (NH₂OH) as an intermediate³⁴. This activity probably establishes an ammonium concentration gradient, extending from the membrane-proximal, ammonium-rich side of the S-layer to areas of lower concentrations near the cell membrane. A previous biophysical model has outlined how such a sink could function¹², potentially initiating a chain of ammonium uptake that provides energy to the cell (Fig. 5c). This passive charge gradient of the S-layer could explain why marine AOA exhibit a 200-fold greater affinity for ammonia compared with ammonia-oxidizing bacteria⁷, which generally lack S-layers. This increased affinity enables AOA to thrive in low-ammonia marine environments. The energy-efficient, passive enrichment mechanism is particularly advantageous in the resource-limited, harsh conditions that are found in the ocean depths. Moreover, as S-layers similar to that of *N. maritimus* are found in nearly all AOA, including those in soil ecosystems (Extended Data Fig. 5a,b), this ammonium enrichment mechanism is probably conserved among these organisms³⁵, contributing to the biogeochemically important nitrogen cycle (Supplementary Fig. 3). A comprehensive understanding of these biogeochemical processes is critical for preserving the vital ecological functions that sustain life on Earth.

Online content

Any methods, additional references, Nature Portfolio reporting summaries, source data, extended data, supplementary information, acknowledgements, peer review information; details of author contributions and competing interests; and statements of data and code availability are available at <https://doi.org/10.1038/s41586-024-07462-5>.

- Könneke, M. et al. Isolation of an autotrophic ammonia-oxidizing marine archaeon. *Nature* **437**, 543–546 (2005).
- Hutchins, D. A. & Capone, D. G. The marine nitrogen cycle: new developments and global change. *Nat. Rev. Microbiol.* **20**, 401–414 (2022).
- Karner, M. B., DeLong, E. F. & Karl, D. M. Archaeal dominance in the mesopelagic zone of the Pacific Ocean. *Nature* **409**, 507–510 (2001).
- Könneke, M. et al. Ammonia-oxidizing archaea use the most energy-efficient aerobic pathway for CO₂ fixation. *Proc. Natl Acad. Sci. USA* **111**, 8239–8244 (2014).
- Kraft, B. et al. Oxygen and nitrogen production by an ammonia-oxidizing archaeon. *Science* **375**, 97–100 (2022).
- Wan, X. S. et al. Ambient nitrate switches the ammonium consumption pathway in the euphotic ocean. *Nat. Commun.* **9**, 915 (2018).
- Martens-Habbena, W., Berube, P. M., Urakawa, H., de la Torre, J. R. & Stahl, D. A. Ammonia oxidation kinetics determine niche separation of nitrifying Archaea and Bacteria. *Nature* **461**, 976–979 (2009).
- Urakawa, H., Martens-Habbena, W. & Stahl, D. A. in *Nitrification* 115–155 (John Wiley & Sons, 2011).
- Qin, W. et al. *Nitrosopumilus maritimus* gen. nov., sp. nov., *Nitrosopumilus cobalaminigenes* sp. nov., *Nitrosopumilus oxycloinae* sp. nov., and *Nitrosopumilus ureiphilus* sp. nov., four marine ammonia-oxidizing archaea of the phylum Thaumarchaeota. *Int. J. Syst. Evol. Microbiol.* **67**, 5067–5079 (2017).
- Bharat, T. A. M., von Kügelgen, A. & Alva, V. Molecular logic of prokaryotic surface layer structures. *Trends Microbiol.* **29**, 405–415 (2021).
- Albers, S. V. & Meyer, B. H. The archaeal cell envelope. *Nat. Rev. Microbiol.* **9**, 414–426 (2011).
- Li, P. N. et al. Nutrient transport suggests an evolutionary basis for charged archaeal surface layer proteins. *ISME J.* **12**, 2389–2402 (2018).
- Li, P. N., Herrmann, J., Wakatsuki, S. & van den Bedem, H. Transport properties of nanoporous, chemically forced biological lattices. *J. Phys. Chem. B* **123**, 10331–10342 (2019).
- Nakagawa, T. & Stahl, D. A. Transcriptional response of the archaeal ammonia oxidizer *Nitrosopumilus maritimus* to low and environmentally relevant ammonia concentrations. *Appl. Environ. Microbiol.* **79**, 6911–6916 (2013).
- Qin, W. et al. Stress response of a marine ammonia-oxidizing archaeon informs physiological status of environmental populations. *ISME J.* **12**, 508–519 (2018).
- von Kügelgen, A. et al. In Situ structure of an intact lipopolysaccharide-bound bacterial surface layer. *Cell* **180**, 348–358 (2020).
- Bharat, T. A. M. et al. Structure of the hexagonal surface layer on *Caulobacter crescentus* cells. *Nat. Microbiol.* **2**, 17059 (2017).
- von Kügelgen, A., Alva, V. & Bharat, T. A. M. Complete atomic structure of a native archaeal cell surface. *Cell Rep.* **37**, 110052 (2021).
- Zivanov, J. et al. A Bayesian approach to single-particle electron cryo-tomography in RELION-4.0. *eLife* **11**, e83724 (2022).
- Jarrell, K. F. et al. N-linked glycosylation in Archaea: a structural, functional, and genetic analysis. *Microbiol. Mol. Biol. Rev.* **78**, 304–341 (2014).
- Herdman, M. et al. High-resolution mapping of metal ions reveals principles of surface layer assembly in *Caulobacter crescentus* cells. *Structure* **30**, 215–228 (2022).
- Baranova, E. et al. SbsB structure and lattice reconstruction unveil Ca²⁺ triggered S-layer assembly. *Nature* **487**, 119–122 (2012).
- von Kügelgen, A. et al. Interdigitated immunoglobulin arrays form the hyperstable surface layer of the extremophilic bacterium *Deinococcus radiodurans*. *Proc. Natl Acad. Sci. USA* **120**, e2215808120 (2023).
- Gambelli, L. et al. Structure of the two-component S-layer of the archaeon *Sulfolobus acidocaldarius*. *eLife* **13**, e84617 (2024).
- Gambelli, L. et al. Architecture and modular assembly of *Sulfolobus* S-layers revealed by electron cryotomography. *Proc. Natl Acad. Sci. USA* **116**, 25278–25286 (2019).
- Fioravanti, A. et al. Structure of S-layer protein Sap reveals a mechanism for therapeutic intervention in anthrax. *Nat. Microbiol.* **4**, 1805–1814 (2019).
- Bharat, T. A. M., Tocheva, E. I. & Alva, V. The cell envelope architecture of *Deinococcus*: HPI forms the S-layer and SlpA tethers the outer membrane to peptidoglycan. *Proc. Natl Acad. Sci. USA* **120**, e2305338120 (2023).
- Kim, J.-G. et al. Spindle-shaped viruses infect marine ammonia-oxidizing thaumarchaea. *Proc. Natl Acad. Sci. USA* **116**, 15645–15650 (2019).
- Song, W. et al. PyLipID: a Python package for analysis of protein-lipid interactions from molecular dynamics simulations. *J. Chem. Theory Comput.* **18**, 1188–1201 (2022).
- Xue, L. et al. Visualizing translation dynamics at atomic detail inside a bacterial cell. *Nature* **610**, 205–211 (2022).
- Tegunov, D., Xue, L., Dienemann, C., Cramer, P. & Mahamid, J. Multi-particle cryo-EM refinement with M visualizes ribosome-antibiotic complex at 3.5 Å in cells. *Nat. Methods* **18**, 186–193 (2021).
- Hollocher, T. C., Tate, M. E. & Nicholas, D. J. Oxidation of ammonia by *Nitrosomonas europaea*. Definite ¹⁸O-tracer evidence that hydroxylamine formation involves a monooxygenase. *J. Biol. Chem.* **256**, 10834–10836 (1981).
- Hodgskiss, L. H. et al. Unexpected complexity of the ammonia monooxygenase in archaea. *ISME J.* **17**, 588–599 (2023).
- Vajrala, N. et al. Hydroxylamine as an intermediate in ammonia oxidation by globally abundant marine archaea. *Proc. Natl Acad. Sci. USA* **110**, 1006–1011 (2013).
- Leininger, S. et al. Archaea predominate among ammonia-oxidizing prokaryotes in soils. *Nature* **442**, 806–809 (2006).
- Buchholz, T.-O. et al. in *Methods in Cell Biology* Vol. 152 (eds Müller-Reichert, T. & Pigino, G.) 277–289 (Academic, 2019).
- Buchholz, T.-O., Jordan, M., Pigino, G. & Jug, F. Cryo-CARE: Content-aware image restoration for cryo-transmission electron microscopy data. In *Proc. 2019 IEEE 16th International Symposium on Biomedical Imaging (ISBI 2019)* 502–506 (IEEE, 2019).
- Sanchez-Garcia, R. et al. DeepEMhancer: a deep learning solution for cryo-EM volume post-processing. *Commun. Biol.* **4**, 874 (2021).
- Schouten, S. et al. Intact membrane lipids of “*Candidatus Nitrosopumilus maritimus*,” a cultivated representative of the cosmopolitan mesophilic group I Crenarchaeota. *Appl. Environ. Microbiol.* **74**, 2433–2440 (2008).

Publisher's note Springer Nature remains neutral with regard to jurisdictional claims in published maps and institutional affiliations.



Open Access This article is licensed under a Creative Commons Attribution 4.0 International License, which permits use, sharing, adaptation, distribution and reproduction in any medium or format, as long as you give appropriate credit to the original author(s) and the source, provide a link to the Creative Commons licence, and indicate if changes were made. The images or other third party material in this article are included in the article's Creative Commons licence, unless indicated otherwise in a credit line to the material. If material is not included in the article's Creative Commons licence and your intended use is not permitted by statutory regulation or exceeds the permitted use, you will need to obtain permission directly from the copyright holder. To view a copy of this licence, visit <http://creativecommons.org/licenses/by/4.0/>.

© The Author(s) 2024

Methods

Growth of *N. maritimus* cells

A culture of *N. maritimus* (SCM1) was provided by F. Elling and A. Pearson. Continuous cultures of SCM1 were grown on modified synthetic *crenarchaeota* medium supplemented with 1 mM NH₄Cl, as previously described^{7,40} at 28 °C in a standing incubator that was covered to prevent excessive exposure to light. The growth of SCM1 *N. maritimus* cells was monitored using a NO₂⁻-detection assay reported previously¹. The same assay was used to follow SCM1 growth with differing ammonium concentrations.

Purification of *N. maritimus* cell envelopes

Native cell envelopes were purified from *N. maritimus* by adapting a previously described protocol²³. A total of 12 l of *N. maritimus* cultures was prepared and late-log-phase cells were collected by centrifugation (10,000g, 4 °C, 30 min) and frozen and stored at -80 °C until further experimentation. The cell pellet from a 1 l culture was carefully resuspended in 3 ml lysis buffer (50 mM HEPES/NaOH pH 7.5, 500 mM NaCl, 50 mM MgCl₂, 10 mM CaCl₂, 1% (w/v) CHAPS, supplemented with 1× cOmplete protease inhibitor cocktail (Roche)). The cell suspension was incubated for 1 h on ice, and then lysed using sonication (10×, 5 s pulse, amplitude strength 10%). The sonicated sample was subsequently centrifuged (80,000g, 4 °C, 1 h), forming a very small white pellet at the bottom of the centrifugation tube. The pellet was resuspended into 40 µl of the same buffer and used for cryo-EM experiments. For the ammonium-enriched sample, the buffer was supplemented with 2.5 mM NH₄Cl.

Cryo-EM and cryo-ET sample preparation

For cryo-EM and cryo-ET grid preparation, previously reported protocols were used^{18,23,41}. In brief, 2.5 µl of the specimen was applied to a freshly glow discharged Quantifoil R2/2 Cu/Rh 200 mesh grid, adsorbed for 60 s, blotted for 4–5 s and plunge-frozen into liquid ethane in the Vitrobot Mark IV (Thermo Fisher Scientific), while the blotting chamber was maintained at 100% humidity at 10 °C. For tomography, the specimen was additionally supplemented with 10 nm gold conjugated with protein A. The grids were clipped and stored under liquid nitrogen until cryo-EM data collection was performed.

Cryo-ET and cryo-EM data collection

Cryo-ET data. For high-resolution in situ structure determination of the S-layer, a pipeline for high-throughput data collection was adopted⁴². In brief, a Titan Krios microscope was used to collect tilt-series data with a dose-symmetric tilting scheme⁴³. Tilt series were collected at a pixel size of 1.327 Å, with a total dose of -121 e⁻ Å⁻² applied over entire series collected between ±60° with 3° tilt increments. A total of 160 tilt series were collected with a defocus range of between -2 and -5 µm target defocus, and the samples were subjected to 0.9 s of exposure per tilt video containing 10 frames each (Extended Data Table 1). For visualization of the cellular ultrastructure, tilt-series images were acquired using the SerialEM software⁴⁴ at a pixel size 3.468 Å with a defocus range of -3 to -10 µm, ±60° oscillation, 1° increments with a total dose of -172 e⁻ Å⁻² as well as at a pixel size of 1.33 Å with a defocus range of -4 to -10 µm, ±60° oscillation, 2° increments with a total final dose of -160 e⁻ Å⁻².

Cryo-EM single-particle data. Single-particle cryo-EM data were collected as described previously^{16,18,23} on the Titan Krios G3 microscope (Thermo Fisher Scientific) operating at 300 kV fitted with a Quantum energy filter (slit width 20 eV) and a K3 direct electron detector (Gatan) with a sampling pixel size of 0.546 Å running in counting super-resolution mode. For the *N. maritimus* purified sheets sample, a total of 12,557 videos over three sessions was collected with a dose rate of around 3.5 e⁻ per super-resolution pixel per s on the camera level. The sample was subjected to 4.2 s of exposure, during which a total dose

of around 48–51 e⁻ Å⁻² was applied, and 40 frames were recorded per video (Extended Data Table 2).

Subtomogram averaging of whole cells for structure determination

To obtain initial lattice maps, a previously described strategy was used¹⁶, in which tilt-series alignment using gold fiducials and tomogram generation was performed using IMOD⁴⁵ and initial contrast transfer functions (CTFs) were estimated using CTFFIND4⁴⁶. Tomograms for visualization were generated using the simultaneous iterative reconstruction technique (SIRT) implemented in Tomo3D⁴⁷ and denoised using Cryo-CARE^{36,37}. Subtomogram averaging was performed using custom scripts written in MATLAB, described in detail elsewhere^{42,48}. For initial cryo-ET structure determination, we used previously published methods¹⁷, with the major difference being the use of a recently developed 3D-CTF correction method for tomographic data⁴⁹. The roughly aligned subtomogram coordinates were then imported into RELION-4 for further analysis¹⁹. We used the tilt series after video frame alignment from the initial analysis above, without additional preprocessing, along with the tilt-series alignments performed within IMOD, CTF parameters from CTFFIND4⁴⁶ and the Euler angle assignments and subtomogram coordinates from the original analysis to proceed with refinement. The imported parameters into RELION-4 were used for multiple cycles of pseudosubtomogram generation and realignment as described recently¹⁹. Accounting for per-particle motions with additional cycles of pseudosubtomogram improvements and realignments increased the resolution of the *Nm*SLP hexamer to 3.4 Å in C₆ symmetry. Relaxation of the symmetry^{50,51} led to an improved (3.3 Å) resolution overall, and 3.2 Å at the pseudo-hexameric axis, but decreased the resolution (-4.5 Å) at the periphery of the hexamer (Extended Data Table 1 and Extended Data Fig. 1). For spatial analysis of hexameric and pentameric S-layer positions with respect to the cell centre, the distance of each position from the cell centre was normalized by the maximally distanced hexamer/pentamer in every cell in the tomogram.

Cryo-EM single-particle analysis

For S-layer structure from two-dimensional sheets, cryo-EM data processing was performed as described previously for S-layers in our laboratory^{18,23}. Videos collected at the scope were clustered into optics groups based on the XML metadata of the data-collection software EPU (Thermo Fisher Scientific) using a *k*-means algorithm implemented in EPU_group_AFIS (https://github.com/DustinMorado/EPU_group_AFIS). Imported videos were motion-corrected, dose-weighted and Fourier cropped (2×) with MotionCor2⁵² implemented in RELION-3.1⁵³. CTFs of the resulting motion-corrected micrographs were estimated using CTFFIND4⁴⁶. Initially, side views of S-layer sheets were first manually picked along the edge of the lattice using the helical picking tab in RELION while setting the helical rise to 60 Å. Top and tilted views were manually picked at the central hexameric axis. Manually picked particles were extracted in 4× downsampled 128 × 128 px² boxes and classified using reference-free 2D classification inside RELION-3.1. Class averages centred at a hexameric axis were used to automatically pick particles inside RELION-3.1. Automatically picked particles were extracted in 4× downsampled 128 × 128 px² boxes and classified using reference-free 2D classification. Particle coordinates belonging to class averages centred at the hexameric axis were used to train TOPAZ⁵⁴ in 5× downsampled micrographs using the neural network architecture conv127. For the final reconstruction, particles were picked using TOPAZ and the previously trained neural network above. Furthermore, top, bottom and side views were picked using the reference-based autopicker inside RELION-3.1, which TOPAZ did not readily identify. Particles were extracted in 4× downsampled 128 px × 128 px boxes and classified using reference-free 2D classification inside RELION-3.1. Particles belonging to class averages centred at the pseudo-hexameric axis were combined, and particles within 30 Å were removed to prevent

duplication after alignment. All of the resulting particles were then re-extracted in $4 \times$ downsampled $128 \times 128 \text{ px}^2$ boxes. All of the side views and a subset of the top and bottom views were used for initial model generation in RELION-3.1. The scaled and low-pass filtered output was then used as a starting model for 3D auto refinement in a $512 \times 512 \text{ px}^2$ box. Per-particle defocus, anisotropy magnification and higher-order aberrations⁵⁵ were refined inside RELION-3.1, followed by three rounds of focused 3D autorefinement. Bayesian particle polishing was performed subsequently in a $640 \text{ px} \times 640 \text{ px}$ box⁵⁵ followed by autorefinement and symmetry relaxation^{50,51}. The final map was obtained from 354,860 particles and post-processed using a soft mask focused on the central hexamer, yielding a global resolution of 2.7 \AA according to the Fourier shell correlation criterion between two independently refined half-maps at a threshold value at 0.143 (ref. 56) and a local resolution of up to 2.5 \AA (Extended Data Fig. 3 and Extended Data Table 2). The two-dimensional sheet-like arrangement led to anisotropy in resolution, with lower resolution perpendicular to the plane as estimated by directional FSCs⁵⁷. Further details are provided in Extended Data Table 2 and Extended Data Fig. 3.

Data visualization, analysis and model building

For model building, a previously described strategy was used^{18,23}. For the single-particle cryo-EM map, the original $640 \times 640 \times 640$ voxel box was cropped into a $320 \times 320 \times 320$ voxel box. In both the cryo-ET and cryo-EM maps, and the protein backbone of *Nm*SLP was manually traced as a poly-alanine model through a single *Nm*SLP subunit using Coot⁵⁸. Side chains were assigned at clearly identifiable positions which allowed deduction of the protein sequence register. The model was then placed into the hexameric map as six copies and subjected to several rounds of refinement using *refmac5*⁵⁹ inside the CCP-EM software suite⁶⁰ and PHENIX⁶¹, followed by manually rebuilding in Coot⁵⁸. At the N terminus, the C_2 maps were better resolved compared to the C_6 maps at the C termini of *Nm*SLPs; therefore, multimap atomic model refinement was performed in *servalcat*⁶². Model validation was performed in PHENIX and CCP-EM, and data visualization was performed in UCSF Chimera⁶³, UCSF ChimeraX⁶⁴ and PyMOL⁶⁵. To analyse lattice interfaces, multiple copies of the hexameric structure were placed in the cryo-EM map prepared with a larger box size. Figure panels containing cryo-EM or cryo-ET images were prepared using IMOD and Fiji⁶⁶. Lattice maps of S-layers for visual inspection were plotted inside UCSF Chimera⁶³ with the PlaceObject plugin⁶⁷ and model coordinates were plotted inside UCSF ChimeraX⁶⁴ with the *sym* function and the BIOMATRIX PDB file header or directly using the ArtiaX plugin⁶⁸. The SPA and STA maps were postprocessed using deepEMhancer³⁸ for visualization of the *N*-glycan densities (Fig. 2k and Extended Data Fig. 4g–h,k–l). Composite maps from focused refinements of the two-fold (C_2) and six-fold (C_6) symmetrized maps were generated using *refmac5*⁵⁹ and PHENIX⁶¹ and then converted using *mtz2mrc* implemented in PHENIX⁶¹.

Bioinformatic analysis

A previously described strategy for detection and analysis of SLPs was used^{18,23}. All sequence similarity searches were performed in the MPI Bioinformatics Toolkit⁶⁹ using BLAST⁷⁰ and HHpred⁷¹. BLAST searches were performed against the *nr_arc* database, a specialized subset of the NCBI non-redundant protein sequence database filtered specifically for archaeal sequences, using the default settings to identify homologues of *Nm*SLP in archaea. The searches were seeded with the protein sequence of *N. maritimus* SLP. The domain organization of several obtained matches and many experimentally characterized SLPs (Supplementary Table 1) were analysed using HHpred searches with the default settings over the PDB70 and ECOD70 databases, which are versions of the PDB and ECOD databases filtered for a maximum pairwise identity of 70%, and using structural models built using AlphaFold (v.2.2.0)⁷². Signal peptides were predicted using SignalP (v.6.0)⁷³.

The mean local charge of the protein sequences was calculated using the EMBOSS charge tool⁷⁴, using a window length of 7.

ITC analysis

ITC measurements were made using Malvern Panalytical ITC200 instruments at $25 \text{ }^\circ\text{C}$ in SCM buffer without ammonium chloride. Experiments were performed at a reference power of $10 \text{ } \mu\text{cal s}^{-1}$ and with injections at 300 s intervals to capture the large exothermic heats and broad peak profiles. The ITC cell contained *N. maritimus* at an optical density at 600 nm (OD_{600}) of 1.0 and the syringe contained 10 mM ammonium chloride in the SCM buffer. In total, ten injections, with the first injection corresponding to $0.5 \text{ } \mu\text{l}$, followed by nine injections of $1 \text{ } \mu\text{l}$ were performed, resulting in a final ammonium chloride concentration of 0.475 mM in the ITC cell. *N. maritimus* cells were pretreated with 0, 2.5 or 5 mM EGTA for 30 min, and were then centrifuged at $16,000g$ for 15 min and resuspended in SCM medium lacking ammonium chloride to recover before adjusting to an OD_{600} of 1.0. Control measurements of injections of ammonium chloride into buffer were performed and these heats were small and close to the values seen for buffer into buffer control experiments. This control heat was subtracted from the *N. maritimus* experiments before peak integration using Malvern Panalytical PEAQ software. Experiments were performed three times with different batches of *N. maritimus* prepared from cells in log-growth phase in SCM medium with 1 mM ammonium chloride as nutrient source. These cultures were centrifuged and resuspended in SCM buffer lacking ammonium chloride before adjusting to an OD_{600} of 1 and loading into the ITC cell.

MD simulations

The *Nm*SLP hexamer structure was prepared for atomistic MD simulation using VMD (v.1.94)⁶⁷. The system was first solvated with TIP3P water molecules and 0.5 M NaCl to mimic the salinity of sea water. Next, 312 ammonium ions (0.1 M NH_4^+) were randomly distributed throughout the solvent, along with an equal number of chloride counter ions to maintain a charge neutral system. Simulation parameters for NH_4^+ were derived through analogy with existing CHARMM parameters for methylammonium. Note that, to better help identify specific ion binding sites, no structural ions apparent from the *Nm*SLP cryo-EM and cryo-ET structures were included. The resulting system contained 566,371 atoms, including 136,236 protein atoms, 141,657 water molecules, 2,246 sodium ions, 1,358 chloride ions and 312 ammonium ions, within a hexagonal box of dimensions $x = y = 217 \text{ \AA}$, $z = 150 \text{ \AA}$ and axial angles $\alpha = \beta = 90^\circ$, $\gamma = 60^\circ$. The geometry of the simulation box was chosen so that the molecular interfaces observed between neighbouring hexamers in our tomography data would be reproduced through the interactions of the *Nm*SLP hexamer with its periodic images in the x – y plane. The system was then subjected to a series of conjugate gradient energy minimizations followed by three 500 ns MD simulations. To prevent potential distortions in the *Nm*SLP hexamer due to the absence of structural ions offsetting its highly negative charge, protein atoms (excluding hydrogens) were harmonically restrained during simulation. Unless otherwise indicated, analyses were performed after disregarding the first 100 ns of each simulation to ensure equilibrium sampling. To assess the robustness of the observed ammonium-binding pattern, we further constructed hexamer systems containing ammonium at concentrations of 0.05 M (156 NH_4^+ ions) and 0.2 M (624 NH_4^+ ions) using an identical procedure, and these systems were subjected to a single 500 ns production simulation. Note that lower concentrations of ammonium ions could not be used due to few total ammonium ions in the box in every simulation. All simulations were conducted using NAMD (v.2.14)⁶⁸ and the CHARMM36 force field³⁸. Production simulations used the NPT ensemble with conditions maintained at 1 atm and 310 K using the Nosé–Hoover Langevin piston and Langevin thermostat, respectively. The r-RESPA integrator scheme was used with an integration time step of 2 fs and SHAKE constraints applied to all hydrogen

atoms. Short-range, non-bonded interactions were calculated every 2 fs with a cut-off of 12 Å; long-range electrostatics were evaluated every 6 fs using the particle-mesh-Ewald method. Further details are provided in Supplementary Table 3.

Reporting summary

Further information on research design is available in the Nature Portfolio Reporting Summary linked to this article.

Data availability

Maps have been deposited at the Electron Microscopy Data Bank under accession codes EMDB-16482, EMDB-16483, EMDB-16484, EMDB-16486, EMDB-16487, EMDB-16489 and EMDB-16492. Model coordinates have been deposited at the Protein Data Bank under accession codes 8C8L, 8C8K, 8C8M, 8C8N, 8C8O and 8C8R. Further details are provided in Extended Data Tables 1 and 2. Source data are provided with this paper.

- Leavitt, W. et al. Archaeal lipid hydrogen isotopes in a marine thaumarchaeon. *Earth Space Sci. Open Arch.* <https://doi.org/10.1002/essoar.10512169.1> (2022).
- von Kügelgen, A., van Dorst, S., Alva, V. & Bharat, T. A. M. A multidomain connector links the outer membrane and cell wall in phylogenetically deep-branching bacteria. *Proc. Natl Acad. Sci. USA* **119**, e2203156119 (2022).
- Wan, W. et al. Structure and assembly of the Ebola virus nucleocapsid. *Nature* **551**, 394–397 (2017).
- Hagen, W. J. H., Wan, W. & Briggs, J. A. G. Implementation of a cryo-electron tomography tilt-scheme optimized for high resolution subtomogram averaging. *J. Struct. Biol.* **197**, 191–198 (2017).
- Mastronarde, D. N. Automated electron microscope tomography using robust prediction of specimen movements. *J. Struct. Biol.* **152**, 36–51 (2005).
- Kremer, J. R., Mastronarde, D. N. & McIntosh, J. R. Computer visualization of three-dimensional image data using IMOD. *J. Struct. Biol.* **116**, 71–76 (1996).
- Rohou, A. & Grigorieff, N. CTFFIND4: fast and accurate defocus estimation from electron micrographs. *J. Struct. Biol.* **192**, 216–221 (2015).
- Agulleiro, J. I. & Fernandez, J. J. Tomo3D 2.0—exploitation of advanced vector extensions (AVX) for 3D reconstruction. *J. Struct. Biol.* **189**, 147–152 (2015).
- Bharat, T. A. M. et al. Cryo-electron tomography of Marburg virus particles and their morphogenesis within infected cells. *PLoS Biol.* **9**, e1001196 (2011).
- Turoňová, B., Schur, F. K. M., Wan, W. & Briggs, J. A. G. Efficient 3D-CTF correction for cryo-electron tomography using NovaCTF improves subtomogram averaging resolution to 3.4 Å. *J. Struct. Biol.* **199**, 187–195 (2017).
- Iica, S. L. et al. Multiple liquid crystalline geometries of highly compacted nucleic acid in a dsRNA virus. *Nature* **570**, 252–256 (2019).
- Abrishami, V. et al. Localized reconstruction in Scipion expedites the analysis of symmetry mismatches in cryo-EM data. *Prog. Biophys. Mol. Biol.* **160**, 43–52 (2021).
- Zheng, S. Q. et al. MotionCor2: anisotropic correction of beam-induced motion for improved cryo-electron microscopy. *Nat. Methods* **14**, 331–332 (2017).
- Zivanov, J. et al. New tools for automated high-resolution cryo-EM structure determination in RELION-3. *eLife* **7**, e42166 (2018).
- Bepler, T. et al. Positive-unlabeled convolutional neural networks for particle picking in cryo-electron micrographs. *Nat. Methods* **16**, 1153–1160 (2019).
- Zivanov, J., Nakane, T. & Scheres, S. H. W. Estimation of high-order aberrations and anisotropic magnification from cryo-EM data sets in RELION-3.1. *IUCr* **7**, 253–267 (2020).
- Scheres, S. H. RELION: implementation of a Bayesian approach to cryo-EM structure determination. *J. Struct. Biol.* **180**, 519–530 (2012).
- Tan, Y. Z. et al. Addressing preferred specimen orientation in single-particle cryo-EM through tilting. *Nat. Methods* **14**, 793–796 (2017).
- Emsley, P., Lohkamp, B., Scott, W. G. & Cowtan, K. Features and development of Coot. *Acta Crystallogr. D* **66**, 486–501 (2010).
- Murshudov, G. N. et al. REFMAC5 for the refinement of macromolecular crystal structures. *Acta Crystallogr. D* **67**, 355–367 (2011).
- Burnley, T., Palmer, C. M. & Winn, M. Recent developments in the CCP-EM software suite. *Acta Crystallogr. D* **73**, 469–477 (2017).
- Liebschner, D. et al. Macromolecular structure determination using X-rays, neutrons and electrons: recent developments in Phenix. *Acta Crystallogr. D* **75**, 861–877 (2019).
- Yamashita, K., Palmer, C. M., Burnley, T. & Murshudov, G. N. Cryo-EM single-particle structure refinement and map calculation using Servalcat. *Acta Crystallogr. D* **77**, 1282–1291 (2021).
- Petterson, E. F. et al. UCSF Chimera—a visualization system for exploratory research and analysis. *J. Comput. Chem.* **25**, 1605–1612 (2004).
- Petterson, E. F. et al. UCSF ChimeraX: structure visualization for researchers, educators, and developers. *Protein Sci.* **30**, 70–82 (2021).
- The PyMOL molecular graphics system v.2.0 (Schrödinger, 2015).
- Schindelin, J. et al. Fiji: an open-source platform for biological-image analysis. *Nat. Methods* **9**, 676–682 (2012).
- Qu, K. et al. Structure and architecture of immature and mature murine leukemia virus capsids. *Proc. Natl Acad. Sci. USA* **115**, E11751–E11760 (2018).
- Ermel, U. H., Arghittu, S. M. & Frangakis, A. S. ArtiaX: an electron tomography toolbox for the interactive handling of sub-tomograms in UCSF ChimeraX. *Protein Sci.* **31**, e4472 (2022).
- Zimmermann, L. et al. A completely reimplemented MPI bioinformatics Toolkit with a new HHpred server at its core. *J. Mol. Biol.* **430**, 2237–2243 (2018).
- Camacho, C. et al. BLAST+: architecture and applications. *BMC Bioinform.* **10**, 421 (2009).
- Steinegger, M. et al. HH-suite3 for fast remote homology detection and deep protein annotation. *BMC Bioinform.* **20**, 473 (2019).
- Jumper, J. et al. Highly accurate protein structure prediction with AlphaFold. *Nature* **596**, 583–589 (2021).
- Teufel, F. et al. SignalP 6.0 predicts all five types of signal peptides using protein language models. *Nat. Biotechnol.* **40**, 1023–1025 (2022).
- Rice, P., Longden, I. & Bleasby, A. EMBOSS: the European Molecular Biology Open Software Suite. *Trends Genet.* **16**, 276–277 (2000).
- Frickey, T. & Lupas, A. CLANS: a Java application for visualizing protein families based on pairwise similarity. *Bioinformatics* **20**, 3702–3704 (2004).
- Kozłowski, L. P. IPC 2.0: prediction of isoelectric point and pKa dissociation constants. *Nucleic Acids Res.* **49**, W285–W292 (2021).

Acknowledgements This work was supported by the Medical Research Council, as part of UK Research and Innovation (programme MC_UP_1201/31 to T.A.M.B., U105184326 to J.L.). T.A.M.B. thanks the Human Frontier Science Program (grant RGY0074/2021), the Vallee Research Foundation, the European Molecular Biology Organization, the Leverhulme Trust and the Lister Institute for Preventative Medicine for support; V.A. thanks A. Lupas for continued support and the Human Frontier Science Program (grant RGY0074/2021); C.K.C. thanks P. Zhang and M. S. P. Sansom for their support as well as funding through the ERC AdG Program (grant 101021133) and a faculty start-up package from the University of Missouri-Columbia Department of Physics. We thank F. Elling and A. Pearson for the gift of a running *N. maritimus* cell culture; R. Rachel, S. H. W. Scheres and J. Zivanov for advice; and T. Darling, J. Grimmer, I. Clayson and J. J. E. Caesar for help with high-performance computing. One dataset for cryo-ET was acquired at the cryo-electron microscopy platform of the European Molecular Biology Laboratory (EMBL) in Heidelberg. This work was partly supported by institutional funds of the Max Planck Society; iNEXT, project number 653706, funded by the Horizon 2020 program of the European Union; and the MRC Laboratory of Molecular Biology Electron Microscopy Facility and Central Oxford Structural Molecular Imaging Centre (COSMIC). Simulations were performed on computational resources provided by HECBioSim, the UK High End Computing Consortium for Biomolecular Simulation, which is supported by the EPSRC (EP/L000253/1), as well as by the Research Computing Support Services division at the University of Missouri-Columbia, which is supported in part by the National Science Foundation (grant CNS-14229294). For the purpose of open access, the MRC Laboratory of Molecular Biology has applied a CC BY public copyright license to any Author Accepted Manuscript version arising.

Author contributions A.v.K., J.L. and T.A.M.B. designed research. A.v.K. S.v.D., L.L.P., Z.F. and T.A.M.B. performed cryo-EM and cryo-ET experiments. C.K.C. and P.J.S. performed MD simulations. A.v.K. and C.B. performed ITC measurements. V.A. performed bioinformatics analyses. A.v.K., C.K.C., S.v.D., V.A., P.J.S. and T.A.M.B. analysed data. A.v.K. and T.A.M.B. wrote the manuscript with the support of all of the authors.

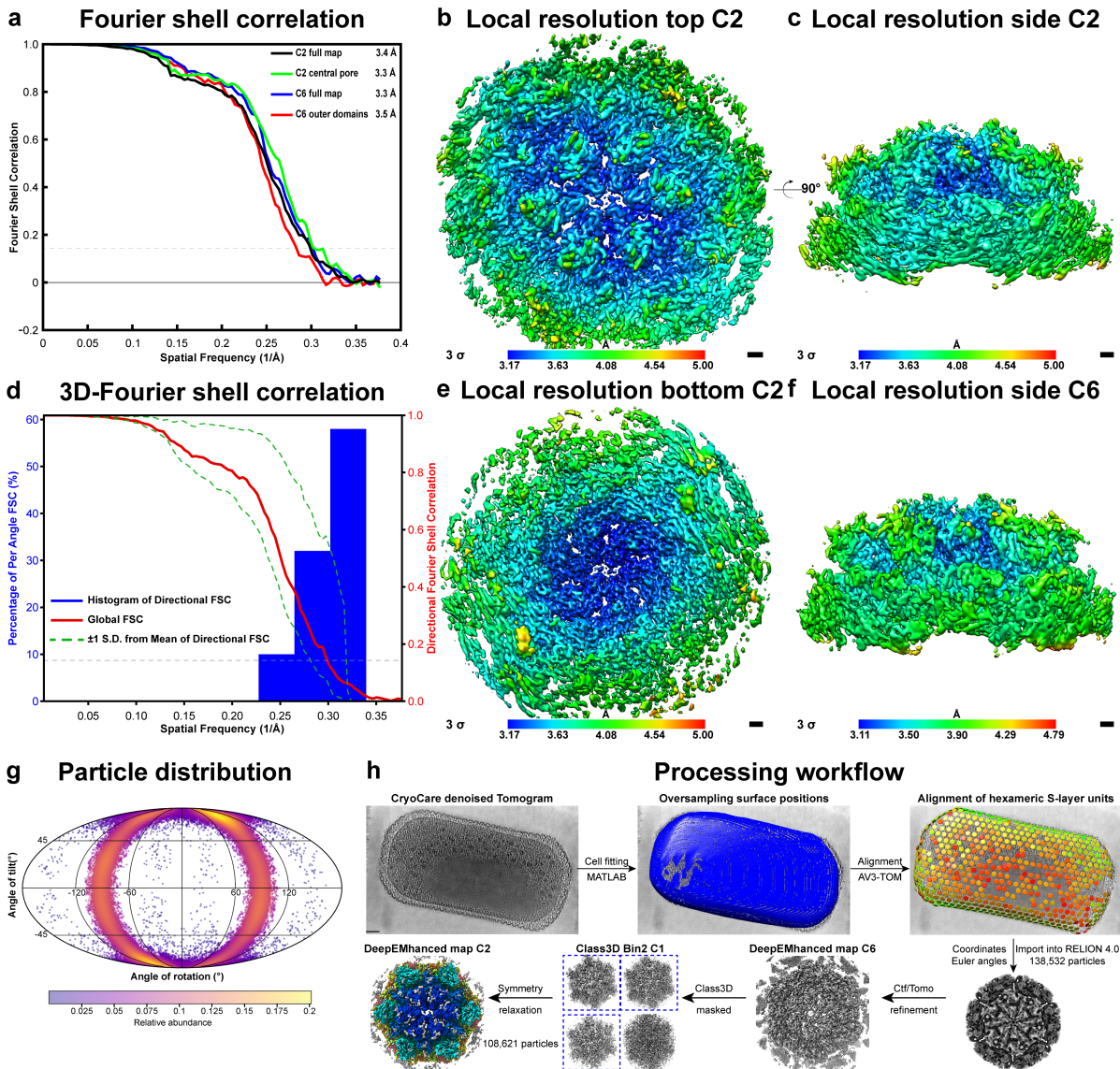
Competing interests The authors declare no competing interests.

Additional information

Supplementary information The online version contains supplementary material available at <https://doi.org/10.1038/s41586-024-07462-5>.

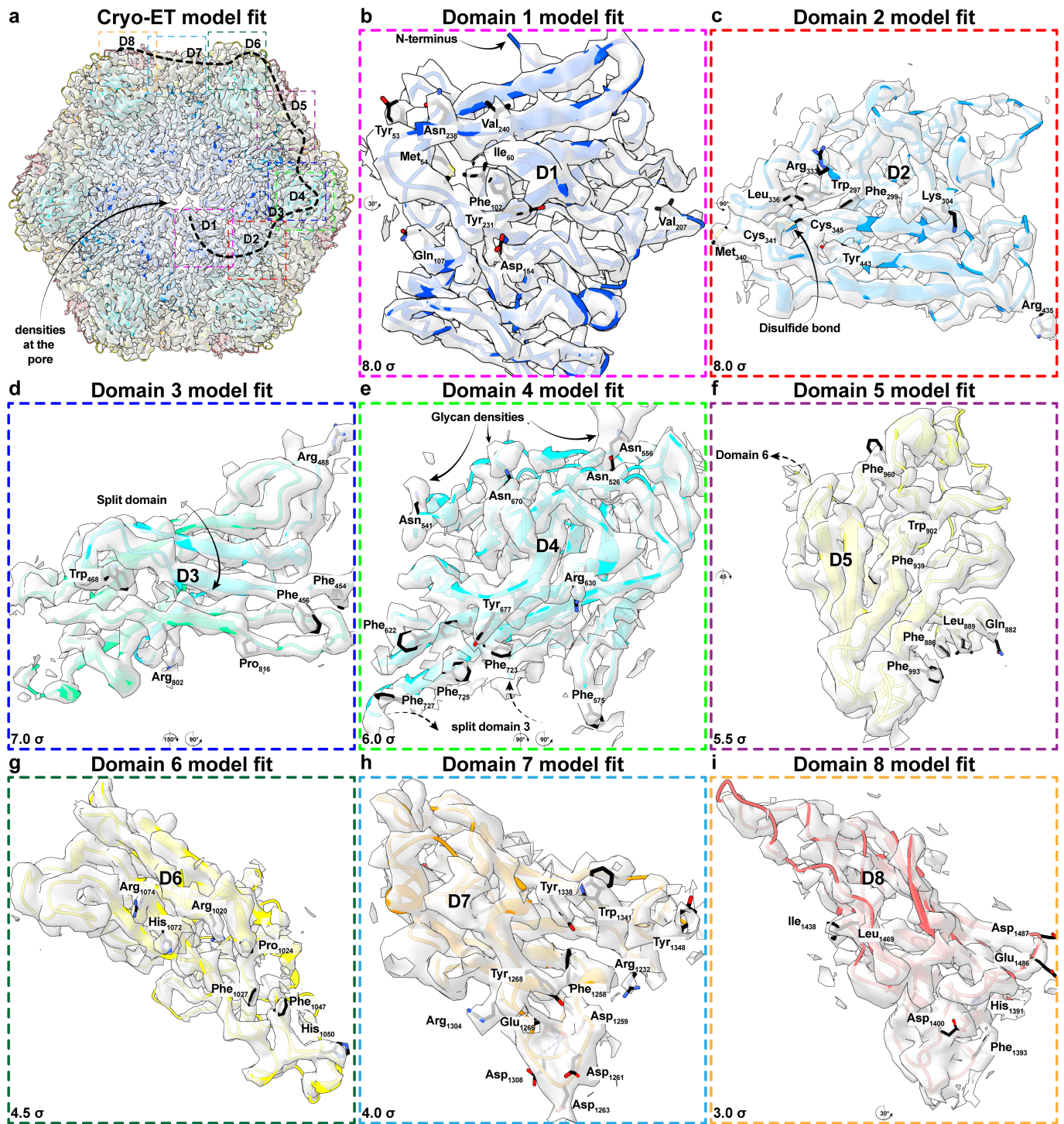
Correspondence and requests for materials should be addressed to Tanmay A. M. Bharat. **Peer review information** Nature thanks Wojciech Kopec, Henry van den Bedem and the other, anonymous, reviewer(s) for their contribution to the peer review of this work. Peer reviewer reports are available.

Reprints and permissions information is available at <http://www.nature.com/reprints>.



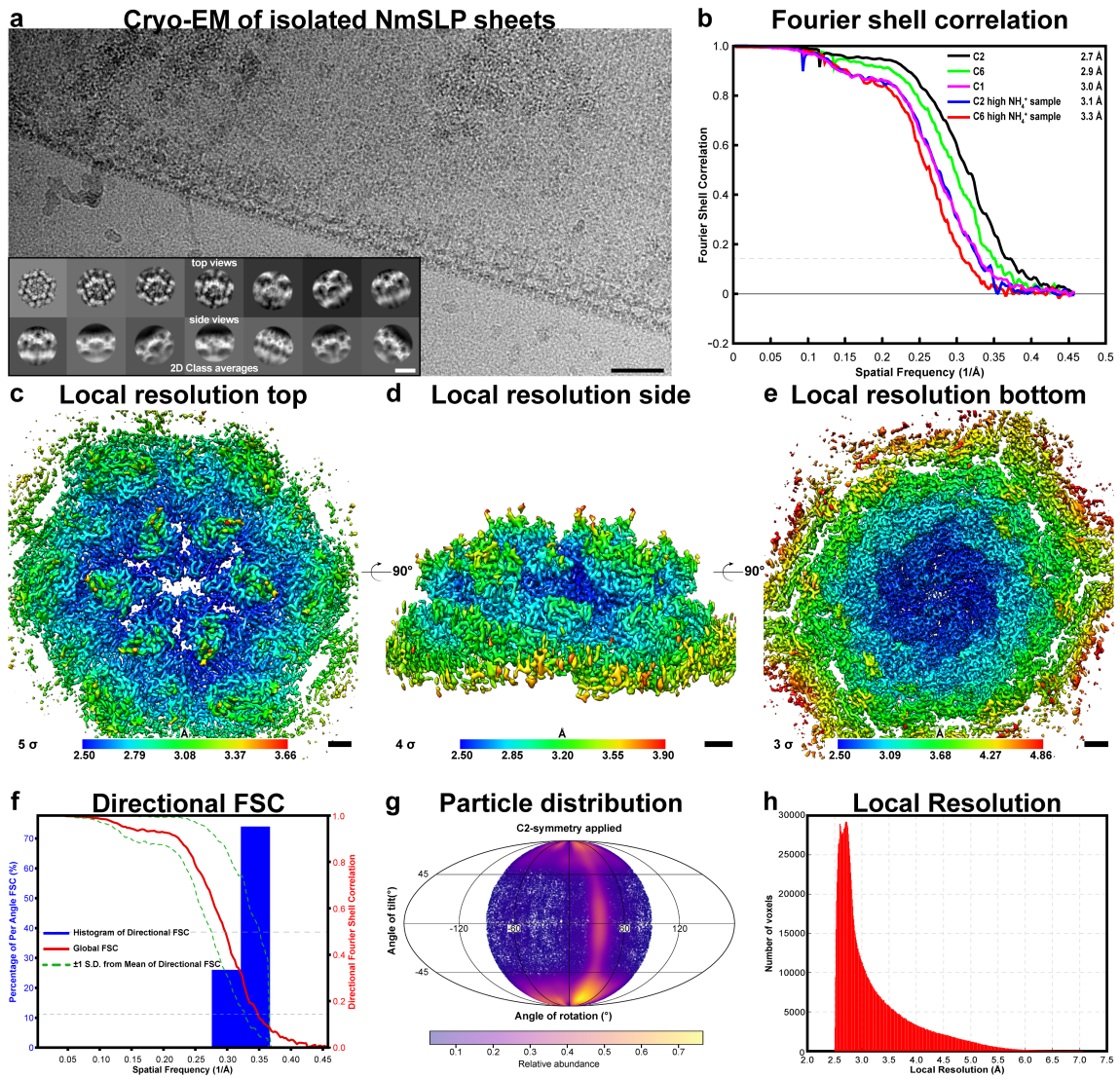
Extended Data Fig. 1 | Subtomogram averaging (STA) of the *N. maritimus* S-layer. **a**, Fourier shell correlation (FSC) curves of the STA reconstruction. **b-c**, Local resolution of two-fold symmetrised (C2) *N. maritimus* S-layer plotted onto the cryo-ET STA map, shown from the top and from the side. **d**, 3-D Fourier shell correlation (FSC) curves of the STA reconstruction. **e**, Local resolution of two-fold symmetrised (C2) *N. maritimus* S-layer shown from the bottom, from

the inside of the cell. **f**, Local resolution of six-fold symmetrised (C6) *N. maritimus* S-layer map shown from the side. **g**, Particle distribution from the 0° projection image. **h**, Processing schematic from tomographic reconstructions to high resolution reconstruction of the S-layer. Scale bars for panels (**b**), (**c**), (**e**) and (**f**): 10 Å.



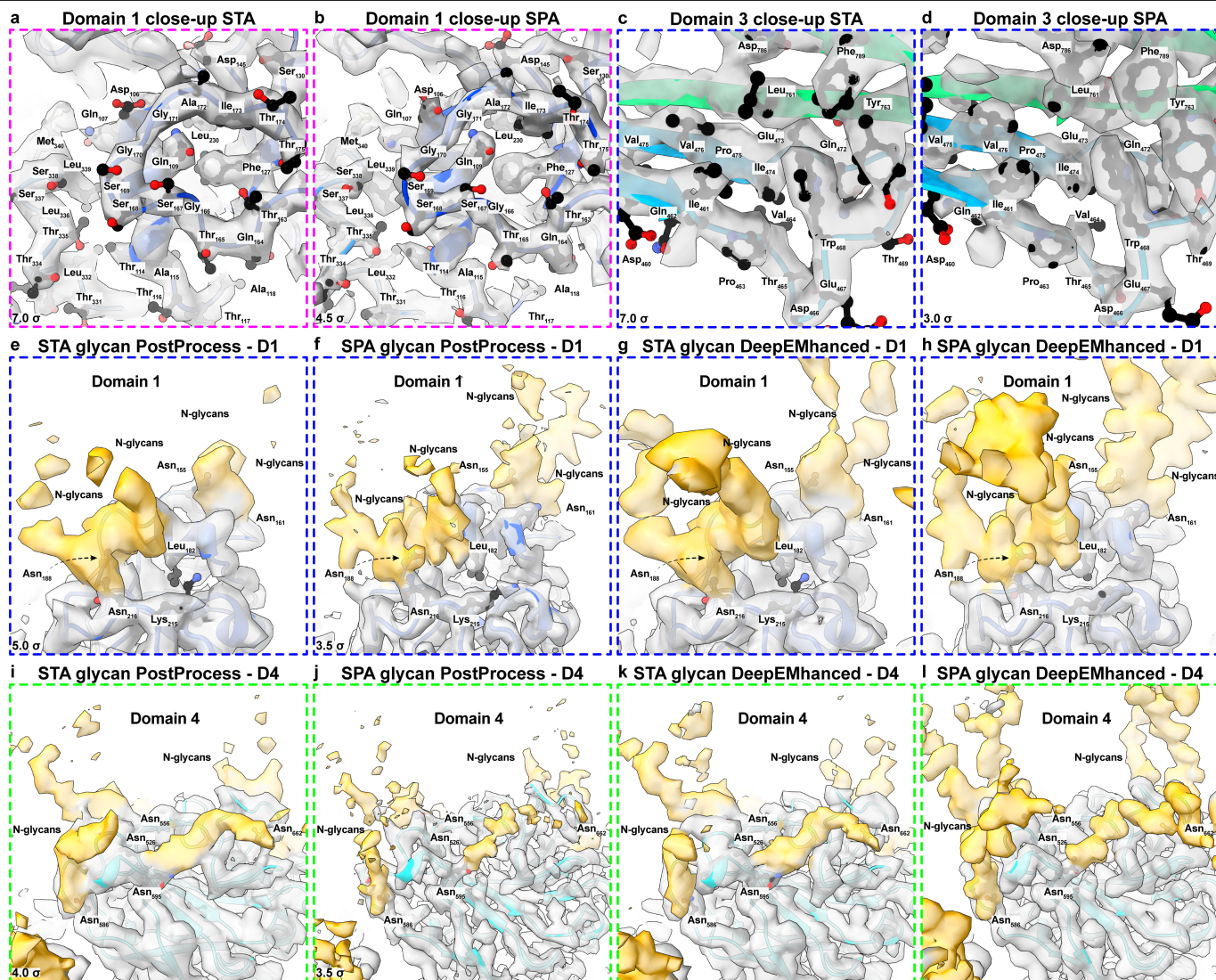
Extended Data Fig. 2 | Structure determination from whole-cell cryo-ET data. **a**, The STA map of the S-layer (isosurface shown) was used to build a model of *Nm*SLP (ribbon) directly from cellular data. (See also Fig. 1(b-e)). **b-i**, Examples

of cryo-ET density and the built model for the Ig-like domains one to eight (D1-D8) of one *Nm*SLP subunit. The local resolution decreases from the central two-fold axis of the *Nm*SLP hexamer (see Extended Data Fig. 1).



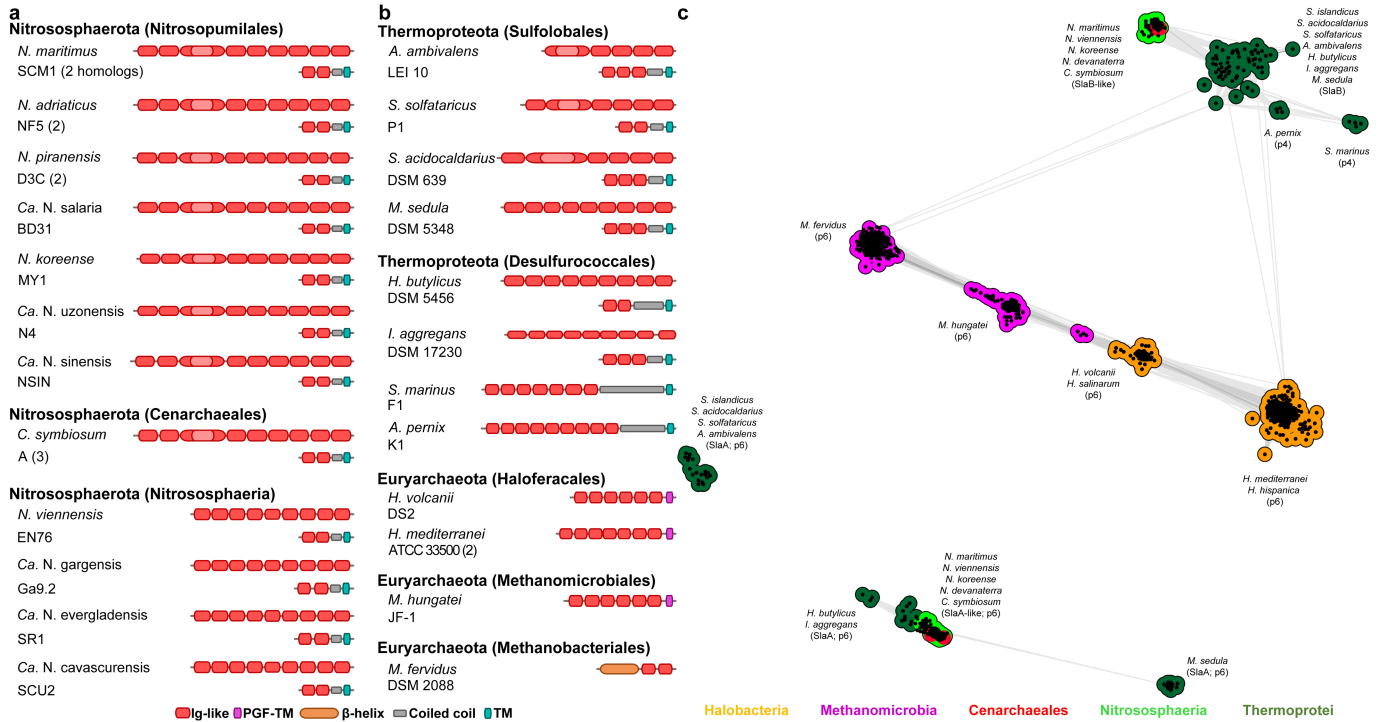
Extended Data Fig. 3 | Single particle analysis of isolated *N. maritimus* S-layer sheets. **a**, Cryo-EM image of isolated *N. maritimus* cell envelopes show repeating units of the pseudo-hexagonal (tilted) S-layer. Insets – characteristic top and side views observed in class averages. This single image is representative from a data set containing 12,557 images from three independent data collections (see Extended Data Table 2). **b**, FSC estimation of the resolution of the unsymmetrized (C1), two-fold (C2) and six-fold (C6) symmetrised maps.

c-e, Local resolution of the C2 cryo-EM map estimated in RELION, plotted into the density, shown in from the top (**c**), side (**d**) and bottom (**e**). The resolution of outer domains (D8-D9) is slightly lower. **f**, Directional 3D-FSC between two random halves of the data⁵⁷. **g**, Angular distribution of the particles in the data set, shown on a relative scale (purple denotes low and yellow denotes high). **h**, Histogram of local resolutions in voxels of the cryo-EM map (C2-symmetrised). Scale bars: (**a**) 500 Å, Inset 200 Å; (**c-d**) 20 Å.



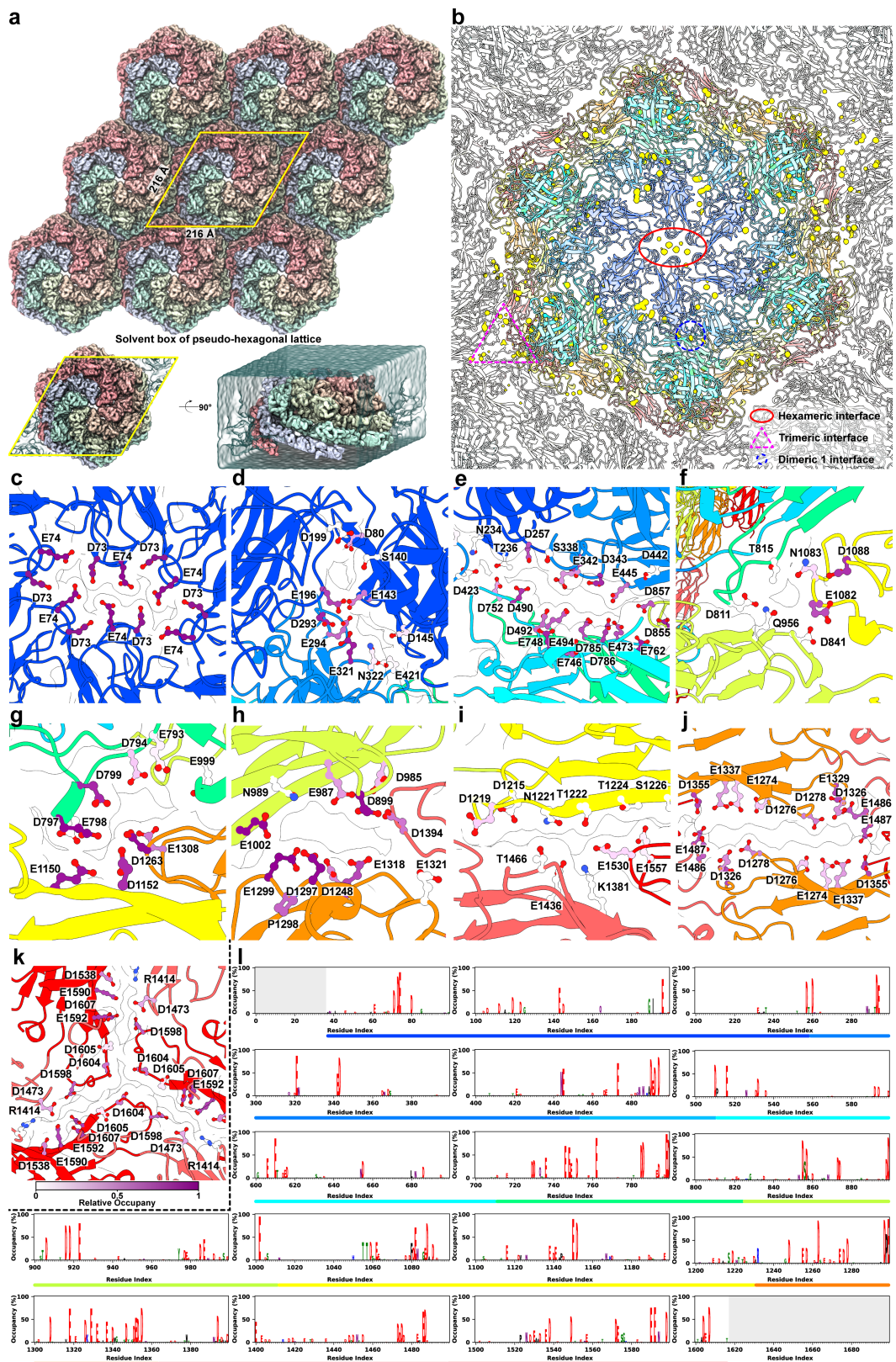
Extended Data Fig. 4 | Comparison of the STA and SPA *N. maritimus* S-layer reconstruction. **a**, Close-up view of the STA map with the built *Nm*SLP model (domain 1) showing resolved large and small side chains. **b**, Close-up view of the SPA map in the same view as shown in panel (a). **c-d**, Close-up view of the STA map (c) and (d) of domain 3 of the *Nm*SLP with resolved small and bulky side

chains. **e-f**, Close-up views of the N-glycan densities of the STA map (a) and SPA map (f) in domain 1. **g-h**, The density of the N-glycans is enhanced in the sharpened³⁸ map (Methods) of the same region. **i-l**, Close-up views of some of the N-glycan densities of the STA (i,k) and SPA map (j,l) of domain 4.



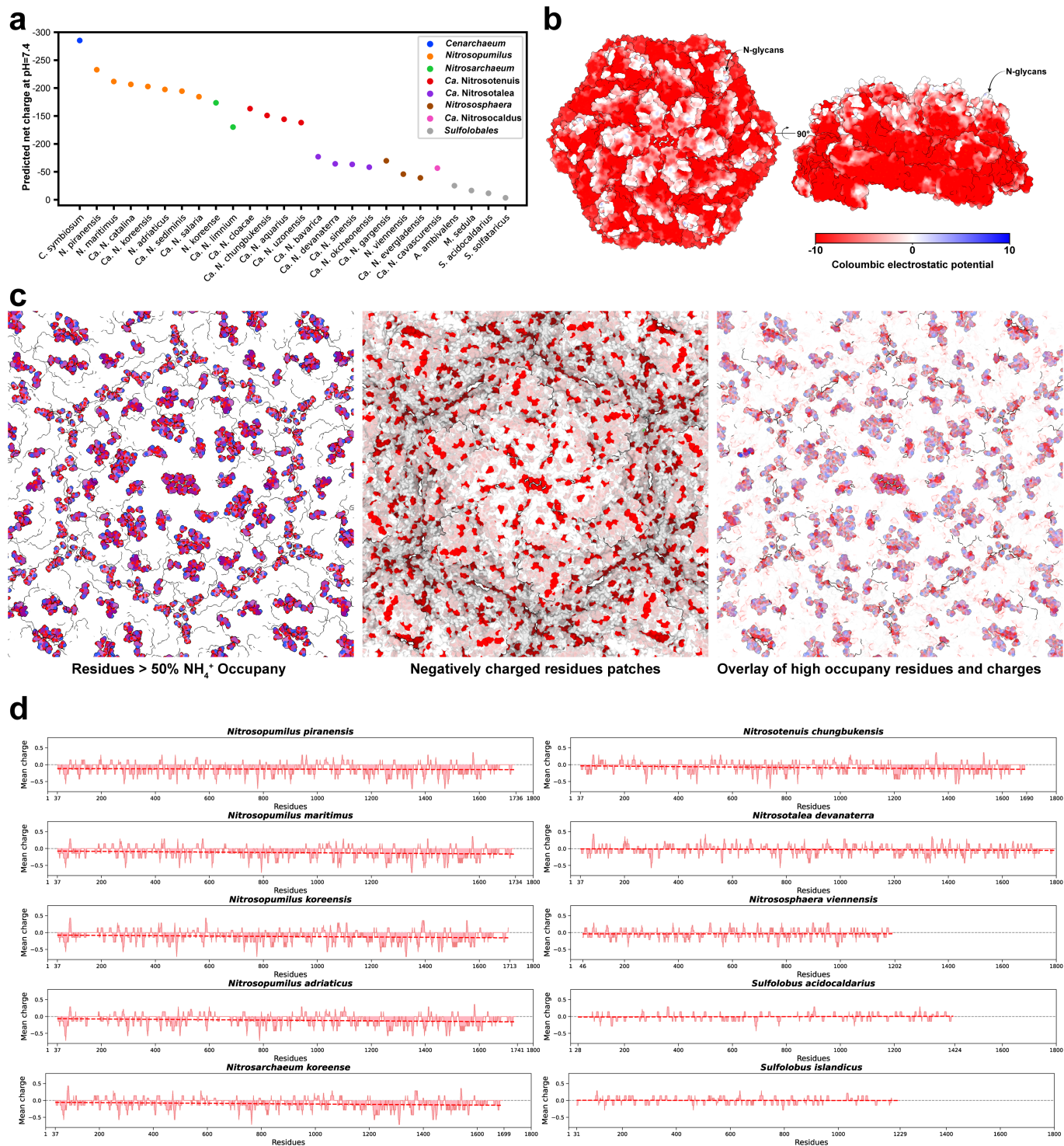
Extended Data Fig. 5 | Bioinformatic analysis of Ig-like domain-containing archaeal SLPs. **a**, Cartoon schematic of the domain architecture of SLPs in Nitrososphaerota. In addition to the main SLP, a minor SlaB homologue is encoded in the genome of most Nitrososphaerota. The SlaB protein exhibits a C-terminal transmembrane domain which potentially anchors the main S-layer canopy to the membrane. **b**, Cartoon schematic of the domain architecture of SLPs in Thermoproteota and Euryarchaeota. The domain architecture of AOA SLPs vary considerably from haloarchaea. **c**, Cluster map of Ig-like domain-containing archaeal SLPs. This map was created by collecting homologues of

various representative Ig-like domain-containing SLPs and clustering them using CLANS²³ based on the strength of their all-against-all pairwise BLAST P-values, with a threshold set at $1-e^{-8}$. Each protein sequence in the map is depicted as a dot, and sequences within the same taxonomic class are denoted by the same colour. The intensity of the line colour indicates the significance of sequence similarities, with darker lines representing higher significance. Although comprising Ig-like domains, archaeal SLPs are extremely divergent in their sequences.



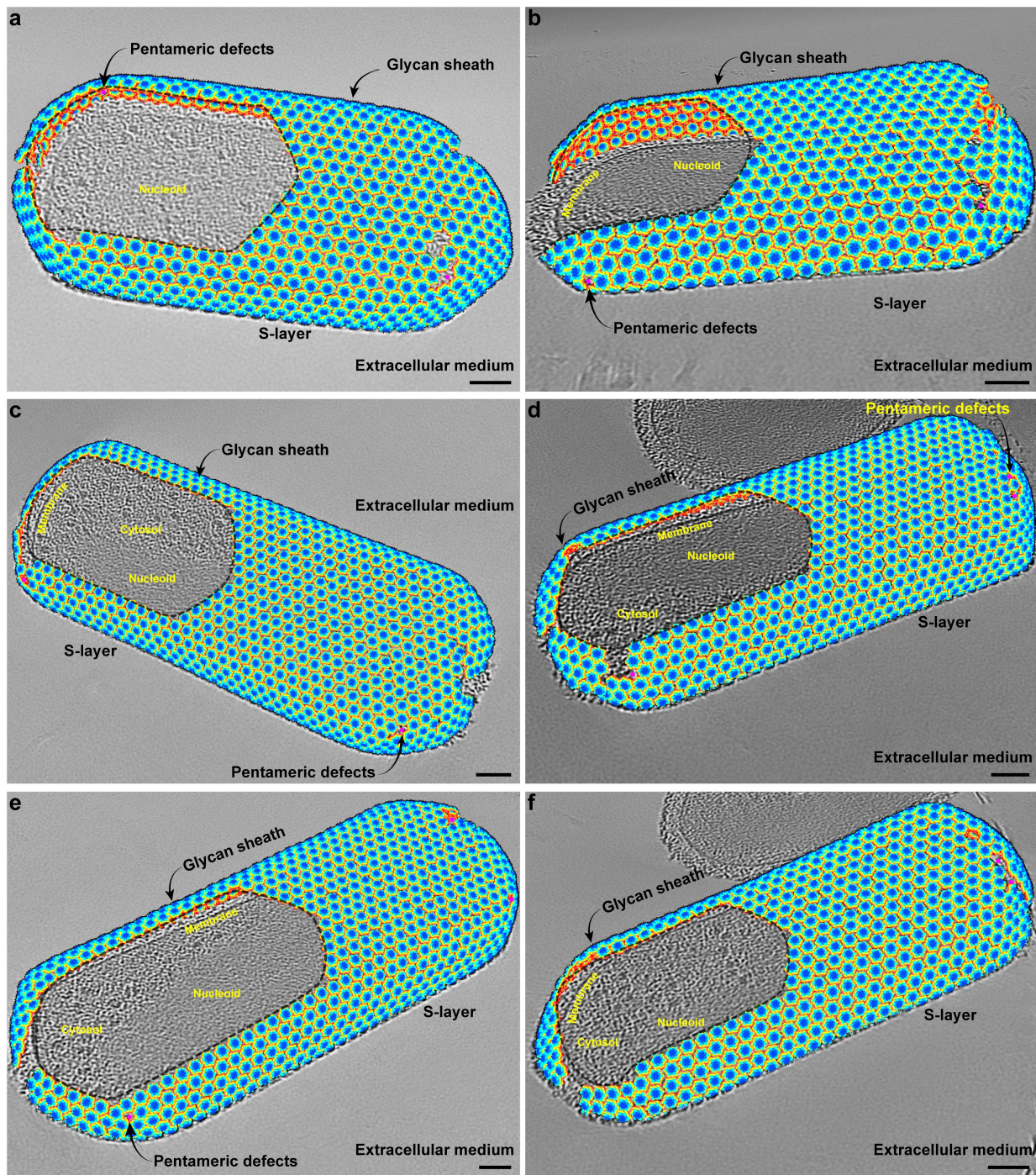
Extended Data Fig. 6 | Molecular dynamics simulation of ammonium ion diffusion across the multi-channel, charged S-layer. a, Unit cell design for MD simulation of the S-layer lattice. The unit cell (simulation box, outlined in yellow) was constructed to simulate an infinite two-dimensional sheet. **b**, Ammonium ion densities (ammonium occupancy during a single simulation shown as golden density) plotted onto the structure shown in ribbon representation. For further details on ammonium binding residues, please see Supplementary Table 2 and

Supplementary Fig. 2. **c-k**, Pores in the S-layer (shown in Fig. 2), with pore residue side chains coloured by occupancy of ammonium ions (colour bar shown in panel k). **l**, Occupancy profile for the modelled *NmSLP* sequence; residues binding to ammonium ions (high occupancy) are shown as large letters. Residue indices corresponding to domains 1 to 9 are depicted by coloured lines below the plot.



Extended Data Fig. 7 | Charge distribution across archaeal S-layers. a, The predicted net charges of archaeal SLPs at neutral pH (7.4) show that *N. maritimus* is highly charged, supporting its function as a cation and ammonium trap. The net charge was calculated using Isoelectric Point Calculator 2.0⁷⁶. **b**, The electrostatic charge of the *N. maritimus* S-layer is illustrated on the surface model. **c**, Residues in the *N. maritimus* S-layer with >50% ammonium occupancy

in MD simulations from pyLipID analysis (left), compared with highlighted negatively charged residues in the S-layer (middle), show a remarkable overlap (right). **d**, The mean local charge of the SLPs from AOAs and other archaea, plotted along the sequence, shows a gradual but continual increase in negative charge specifically in AOAs, but not in other archaea.



Extended Data Fig. 8 | Whole cell tomography of *N. maritimus* and S-layer lattice maps. a-f, Gallery of lattice maps of the S-layer from subtomogram averaging plotted onto denoised^{36,37} *N. maritimus* cellular tomograms (only one slice shown in each case). The S-layer lattice coats nearly the entire outer surface of *N. maritimus* cells. A region has been cut out from each lattice map

on top of the cell for clarity. The hexagonal lattice is joined together by pentameric defects, and linear lattice dislocations are also occasionally observed. Scale bars: 500 Å. Cellular tomography was performed at least 32 times (see Extended Data Table 1).

Article

Extended Data Table 1 | Cryo-ET data collection, refinement, and validation statistics

	Nmar_NmSLP_cryoET	<i>N. maritimus</i> S-layer lattice maps	<i>N. maritimus</i> S-layer lattice maps
Data collection			
Microscope	Titan Krios	Titan Krios	Titan Krios
Detector	K2 (Gatan)	K3 (Gatan)	K3 (Gatan)
Software	SerialEM ⁴⁰	SerialEM ⁴⁰	SerialEM ⁴⁰
Magnification	105,000	64,000	26,000
Voltage (kV)	300	300	300
Slit width (eV)	20	20	20
Defocus range (µm)	-2 to -5	-2 to -10	-3.5 to -10
Pixel size (Å)	1.327	1.33	3.468
Total exposure (e ⁻ /Å ²)	121.36	159.	170.9
Exposure per tilt (e ⁻ /Å ²)	2.96	2.62	1.425
Total number of tilts	41	61	121
Frames per tilt-movie	10	10	3
Tilt increment	±3°	±2°	±1°
Tilt-series scheme	dose-symmetrical	dose-symmetrical	dose-symmetrical
Tilt range	±60°	±60°	±60°
Tilt-series collected	160	27	32
Tilt-series used	153	27	32
Data processing			
Software tilt-series alignment	IMOD ⁴¹	IMOD ⁴¹	IMOD ⁴¹
Software CTF estimation	CTFFIND ⁴²	CTFFIND ⁴²	CTFFIND ⁴²
Software initial angle assignment	AV3-TOM	AV3-TOM	AV3-TOM
Software tilt-series refinement	RELION4.0 ¹⁹	RELION4.0 ¹⁹	RELION4.0 ¹⁹
Software final angle assignment	RELION4.0 ¹⁹	RELION4.0 ¹⁹	RELION4.0 ¹⁹
Software reconstruction	RELION4.0 ¹⁹	RELION4.0 ¹⁹	RELION4.0 ¹⁹
Initial particle images (no.)	138,532		
Final particle images (no.)	108,621		
Pre-cropped Box-size (px)	640 x 640 x 640		
Final Box-size (px)	200 x 200 x 200		
Pixel size final rec. (Å)	1.327		
Symmetry imposed	C2	C6	
Map resolution (Å)	3.35	3.4	
FSC threshold	0.143	0.143	
Map resolution range (Å)	3.2-5.0	3.1-4.8	
Map sharpening <i>B</i> factor (Å ²)	-66.19	-72.45	
3DFSC sphericity [#]	0.94	Not performed	
EMDB code	16487	16489	
Composite map EMDB		16492	
Model Refinement			
Initial model used (PDB code)	None	None	
Software	PHENIX ⁵⁹	PHENIX ⁵⁹	
Model resolution (Å)	3.6	3.9	
FSC threshold	0.5	0.5	
Model composition			
Residue range	37-445	446-1498	
Domain range	D1-D2	D3-D8	
Non-hydrogen atoms	18,347	47,310	
Protein residues	2,508	6,318	
<i>B</i> factors (Å²)			
Protein	74.25	91.26	
R.m.s. deviations			
Bond lengths (Å)	0.002	0.002	
Bond angles (°)	0.503	0.476	
Validation			
MolProbity score	1.74	1.62	
Clashscore	8.26	8.88	
Poor rotamers (%)	0.00	1.14	
Cβ outliers (%)	0.00	0.00	
CABLAM outliers (%)	1.41	1.72	
Ramachandran plot			
Favoured (%)	95.79	97.53	
Allowed (%)	4.21	2.47	
Disallowed (%)	0.00	0.00	
PDB code	8C8N	8C8O	
Composite PDB code		8C8R	

Extended Data Table 2 | Cryo-EM data collection, refinement, and validation statistics

	NmSLP <i>in vitro</i> isolated S-layer			NmSLP high NH ₄ ⁺	
Data collection					
Microscope	Titan Krios	Titan Krios	Titan Krios	Titan Krios	Titan Krios
Detector	K3 (Gatan)	K3 (Gatan)	K3 (Gatan)	K3 (Gatan)	K3 (Gatan)
Software	EPU	EPU	EPU	EPU	EPU
Magnification	81,000	81,000	81,000	81,000	81,000
Voltage (kV)	300	300	300	300	300
Electron exposure (e ⁻ /Å ²)	48.5	50.782	51.543	49.863	49.863
Slit width (eV)	20	20	20	20	20
Defocus range (μm)	-1 to -3	-1.5 to -2	-1 to -1.75	-0.5 to -1.75	-0.75 to -2
Acquisition Mode	Super-res	Super-res	Super-res	Super-res	Super-res
Pixel size (Å)	0.546	0.546	0.546	0.546	0.546
Stage tilt	0°	33°	0°	0°	30°
Movies collected	2,615	3,700	6,242	6,636	2,799
Movies used	2,575	3,620	5,455	6,636	2,799
Frames per movie	40	40	40	40	40
Data processing					
Software picking	TOPAZ ⁵²	TOPAZ ⁵²	TOPAZ ⁵²	TOPAZ ⁵²	TOPAZ ⁵²
Software reconstruction	RELION3.1	RELION3.1	RELION3.1	RELION3.1	RELION3.1
Initial particle images (no.)	926,803	574,714	470,391	1,323,405	776,676
Final particle images (no.)	120,579	119,603	114,678	175,787	41,881
Rescaled Box-size Class2D (px)	128 x 128	128 x 128	128 x 128	128 x 128	128 x 128
Final refinement Box-size (px)		640 x 640 x 640		640 x 640 x 640	
Pixel size final reconstruction (Å)		1.092		1.092	
Final Box-size (px)		640 x 640 x 640		640 x 640 x 640	
Final particle images (no.)		354,860		217,668	
Symmetry imposed	C1	C2	C6	C2	C6
Map resolution (Å)	3.04	2.71	2.87	3.05	3.26
FSC threshold	0.143	0.143	0.143	0.143	0.143
Map resolution range (Å)		2.5 – 3.66	2.5-3.90	2.85-5.01	2.87-4.36
Map sharpening <i>B</i> factor (Å ²)	-46.2	-41.4	-59.2	-52.5	-63.77
EMDB code		16483	16482	16486	
Composite EMDB code		16484			
Model Refinement					
Initial model used (PDB code)		None	None		
Software		Refmac ⁵⁷	Refmac ⁵⁷		
Model resolution (Å)		2.9	3.1		
FSC threshold		0.5	0.5		
Model composition					
Residue range		37-1364	1365-1616		
Domain range		D1-D7	D8-D9		
Non-hydrogen atoms		59,076	11,430		
Protein residues		7,962	1,518		
<i>B</i> factors (Å ²)					
Protein		76.62	118.80		
R.m.s. deviations					
Bond lengths (Å)		0.014	0.013		
Bond angles (°)		1.687	1.619		
Validation					
MolProbity score		1.71	1.55		
Clashscore		7.99	10.8		
Poor rotamers (%)		0.76	0.63		
Cβ outliers (%)		0.33	0.00		
CABLAM outliers (%)		1.98	0.80		
Ramachandran plot					
Favoured (%)		95.95	98.07		
Allowed (%)		4.05	1.93		
Disallowed (%)		0.00	0.00		
PDB Code		8C8L	8C8K		
Composite PDB code		8C8M			

Reporting Summary

Nature Portfolio wishes to improve the reproducibility of the work that we publish. This form provides structure for consistency and transparency in reporting. For further information on Nature Portfolio policies, see our [Editorial Policies](#) and the [Editorial Policy Checklist](#).

Statistics

For all statistical analyses, confirm that the following items are present in the figure legend, table legend, main text, or Methods section.

n/a Confirmed

- The exact sample size (n) for each experimental group/condition, given as a discrete number and unit of measurement
- A statement on whether measurements were taken from distinct samples or whether the same sample was measured repeatedly
- The statistical test(s) used AND whether they are one- or two-sided
Only common tests should be described solely by name; describe more complex techniques in the Methods section.
- A description of all covariates tested
- A description of any assumptions or corrections, such as tests of normality and adjustment for multiple comparisons
- A full description of the statistical parameters including central tendency (e.g. means) or other basic estimates (e.g. regression coefficient) AND variation (e.g. standard deviation) or associated estimates of uncertainty (e.g. confidence intervals)
- For null hypothesis testing, the test statistic (e.g. F , t , r) with confidence intervals, effect sizes, degrees of freedom and P value noted
Give P values as exact values whenever suitable.
- For Bayesian analysis, information on the choice of priors and Markov chain Monte Carlo settings
- For hierarchical and complex designs, identification of the appropriate level for tests and full reporting of outcomes
- Estimates of effect sizes (e.g. Cohen's d , Pearson's r), indicating how they were calculated

Our web collection on [statistics for biologists](#) contains articles on many of the points above.

Software and code

Policy information about [availability of computer code](#)

Data collection

Data analysis

For manuscripts utilizing custom algorithms or software that are central to the research but not yet described in published literature, software must be made available to editors and reviewers. We strongly encourage code deposition in a community repository (e.g. GitHub). See the Nature Portfolio [guidelines for submitting code & software](#) for further information.

Data

Policy information about [availability of data](#)

All manuscripts must include a [data availability statement](#). This statement should provide the following information, where applicable:

- Accession codes, unique identifiers, or web links for publicly available datasets
- A description of any restrictions on data availability
- For clinical datasets or third party data, please ensure that the statement adheres to our [policy](#)

Maps have been deposited in the Electron Microscopy Data Bank (EMDB) and atomic coordinates have been deposited in the Protein Data Bank (PDB). The accession codes are: In vitro S-layer structure (single particle analysis, SPA) with two-fold symmetry (C2): PDB ID 8C8L, EMD-16483; In vitro S-layer structure (SPA) with two-

fold symmetry (C6): PDB ID 8C8K, EMD-16482; In vitro S-layer structure (SPA) composite map: PDB ID 8C8M, EMD-16484; In vitro S-layer structure (SPA) with high NH4Cl and two-fold symmetry (C2): EMD-16486; In situ S-layer structure (subtomogram averaging, STA) with two-fold symmetry (C2): PDB ID 8C8N, EMD-16487; In situ S-layer structure (STA) with two-fold symmetry (C6): PDB ID 8C8O, EMD-16489; In situ S-layer structure (STA) composite map: PDB ID 8C8R, EMD-16492; For more details see Extended Data tables 1 and 2, respectively. No new sequences are reported in this study.

Research involving human participants, their data, or biological material

Policy information about studies with [human participants or human data](#). See also policy information about [sex, gender \(identity/presentation\), and sexual orientation](#) and [race, ethnicity and racism](#).

Reporting on sex and gender	Not applicable
Reporting on race, ethnicity, or other socially relevant groupings	Not applicable
Population characteristics	Not applicable
Recruitment	Not applicable
Ethics oversight	Not applicable

Note that full information on the approval of the study protocol must also be provided in the manuscript.

Field-specific reporting

Please select the one below that is the best fit for your research. If you are not sure, read the appropriate sections before making your selection.

Life sciences Behavioural & social sciences Ecological, evolutionary & environmental sciences

For a reference copy of the document with all sections, see [nature.com/documents/nr-reporting-summary-flat.pdf](https://www.nature.com/documents/nr-reporting-summary-flat.pdf)

Life sciences study design

All studies must disclose on these points even when the disclosure is negative.

Sample size	Cryo-EM and cryo-ET data set sizes were selected to obtain high-resolution reconstructions. The sample size was chosen to reach a resolution of 3.3-4.5 Å for the cryoET data and 2.7 Å for cryoEM data.
Data exclusions	Cryo-EM micrographs and tilt-series were selected based on high resolution content in the cryo-EM or cryo-ET workflow. Extracted particles not suitable for high-resolution reconstruction were excluded during the processing. For further details on image selection see Extended Data Tables 1 and 2.
Replication	The structures were solved as per the accepted protocols for data analysis, including an unbiased Fourier Shell correlation of independently aligned and averaged halves of the data. Triplicate experiments were performed for molecular simulations and growth curves, all replicates showed the same results. Other experiments like ITC were performed in triplicates. All replicates showed similar results.
Randomization	Not relevant to this study. Randomisation was not needed for the statistics.
Blinding	Not relevant to this study. Not needed for the statistics.

Reporting for specific materials, systems and methods

We require information from authors about some types of materials, experimental systems and methods used in many studies. Here, indicate whether each material, system or method listed is relevant to your study. If you are not sure if a list item applies to your research, read the appropriate section before selecting a response.

Materials & experimental systems

- n/a | Involved in the study
- Antibodies
- Eukaryotic cell lines
- Palaeontology and archaeology
- Animals and other organisms
- Clinical data
- Dual use research of concern
- Plants

Methods

- n/a | Involved in the study
- ChIP-seq
- Flow cytometry
- MRI-based neuroimaging

Plants

Seed stocks

Not relevant to this study.

Novel plant genotypes

Not relevant to this study.

Authentication

Not relevant to this study.